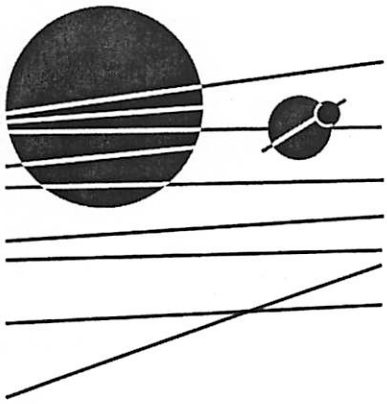

DEPARTMENT OF PLANETARY SCIENCES

LUNAR AND PLANETARY LABORATORY

THE UNIVERSITY OF ARIZONA

Southern New Mexico

Wind and Fire

PtyS 594: Planetary Geology Field Practicum
October 20-22, 2007

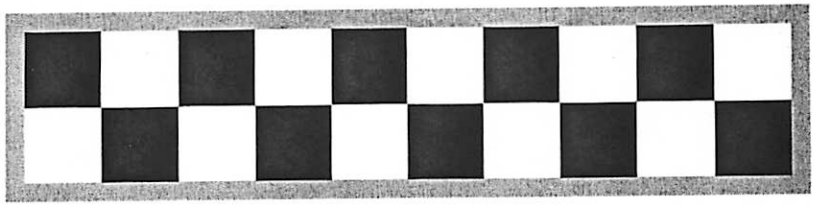

Southern New Mexico, Fall 2007
PtyS 594 Fieldtrip Guidebook

Table of Contents

PtyS 594a,

PLANETARY FIELD GEOLOGY PRACTICUM

Fall 2007 Wind and Fire in Southern New Mexico

Approximate Itinerary

Saturday, 20 October

8:00 AM Depart LPL loading dock. Travel South on Campbell to I-10, proceed East in the direction of El Paso.

9:00 AM Stop at the Texas Canyon rest area on I-10, proceed to the East end and get out at the prominent outcrop of rounded boulders. **Tom Schad** will inform us about how these Spheroidally weathered rocks form, and compare them to possible examples on Mars and Titan.

9:45AM Continue East on I-10 toward New Mexico.

12:00 AM Lunch stop in vicinity of Deming, New Mexico, most likely at the Municipal Park, just off the freeway exit.

12:45 PM Continue East on I-10 toward El Paso.

Three Routes to Kilbourne Hole:

From I-10, between Deming and Las Cruces (long, not the best route)
- Turn S on frontage road at exit 116
- Follow road B4 to intersection with A17
- Turn S of vicinity of Kilbourne Hole

From La Union, New Mexico
- Proceed to NW edge of town
- At the fork, take Dona Ana County Road A-020 on the left of the fork
- Proceed W on A-020 to the RR tracks
- Cross RR tracks, turn right at the T
- Proceed NW
- Cross 2 cattle guards, then turn left on the second road, Dona Ana County Road A-011
- Proceed W on A-011
- Pass A-016 and A-015 intersections; Continue W to Kilbourne Hole

From El Paso, Texas

0.0 mi	Mesa St. (Route 20) and I-10 Drive W on Mesa St., which becomes Country Club Rd. Stay on TX-260 at fork with TX-20 (2.5 mi)
2.5 mi	State Line. Continue straight on Route 1884, entering NM (0.7 mi)
3.2 mi	At junction with NM-273, turn right (1.6 mi)
4.8 mi	Turn left at junction with Santa Teresa Aeropuerto; Dona Ana County NM A-17 (2.6 mi)
7.4 mi	Turn left on paved road at sign for John Nobles, Inc. (pink stripe on building; 0.3 mi)
7.7 mi	Dirt road begins (0.1 mi)
7.8 mi	Bear right at fork, just after RR tracks (0.85 mi)
8.65 mi	Junction AC-3; bear right at fork; RR tracks on right (0.55 mi)
9.2 mi	Cross cattleguard (4.8 mi)
14.0 mi	Cross cattleguard; turn left toward JCJ Ranch, Mount Riley and East Portillo Mountains ahead on the horizon until next turn (10.2 mi)
24.2 mi	Road passes over first flows of the Afton-Aden volcanic field (1.1 mi)
25.3 mi	Pass road on right (0.3 mi)
25.6 mi	Turn right towards Hunt's Hole on prominent dirt road; continue around left side on graded road (1.3 mi)
26.9 mi	Gate (close after passing through, if closed at approach; 1.0 mi)
27.9 mi	Push-up lava flow on the right, ahead (1.7 mi)
29.6 mi	South end of Kilbourne Hole

3:30 PM Arrive Kilbourne Hole. Climb to rim of crater for an overlook. **Doug Archer** will describe the appearance of Kilbourne hole and other maar volcanoes from space. **Andrea Philippoff** will tell us about the general situation of magmatism in the Rio Grande Rift, and **Eric Palmer**, if he can join us, will describe the mineralogy of the crust and upper mantle beneath us.

5:00 PM Set up camp. After dinner **Kat Volk** will regale us about Robert Goddard and the first space rockets.

Sunday, October 21

8:00 AM Break Camp and prepare for a short hike (water, sunscreen, hats, etc.)

8:30 AM Hike partway around E side of Kilbourne hole, collecting crustal and mantle xenoliths along the way. Back at camp, assemble a stratigraphic column with samples all have collected. **Mike Bland** will describe the scientific interpretation of these mantle xenoliths

11:30 AM Lunch at Kilbourne Hole.

12:15 PM Return to I-10 and proceed to Las Cruces. In Las Cruces, pick up Route 70, traveling East towards Alamogordo.

1:30 PM Stop on Route 70 at the Organ Mountains overlook. **Devin Schrader** will use this magnificent overlook to tell us about the tectonics of the Rio Grande rift, on whose Eastern margin we are standing. **Lissa Ong** may be persuaded to say a few words about the White Sands missile range spread out at our feet to the East.

2:00 PM Continue East on Route 70, to the exit for the White Sands National Monument.

2:45 PM Arrive at White Sands National Monument, wait at the gate for our fee wavier to be accepted, then proceed North to the parking lot in the interdune area. Climb a convenient dune, then listen to **Robin Van Auken**, who will described the source of the gypsum sands here and possibly on Mars. **Serina Diniega** will tell us about the mechanics of dune and ripple formation on the Earth and elsewhere. **Catherine Niesh** will follow with a discussion of how dunes appear to synthetic aperture radar (used in imaging Venus and Titan) and explain how radar can be used to determine dune slopes.

4:30 PM Depart White Sands and continue East on Route 70, to Alamogordo, then turn North onto Route 54 toward Carrizozo. At Carrizozo, proceed 4 miles West on Rte 380 to the Valley of Fires state campground.

6:00 PM Arrive at the Valley of Fires campground. Make camp. After dinner we will hear from **David Choi** about the first atomic bomb test just a few miles West of our campground—Trinity.

Monday, 22 October

8:00 AM Walk out onto the rugged surface of the Carrizozo lava flow (good shoes will be a great help here!) and find a comfortable spot to learn about the eruption and emplacement of the flow from **Guo Fan**. Then **Colin Dundas** will explain the latest and best theories of how pahoehoe lava flows work, and **Lissa Ong** will follow this with a discussion of how lava

flows choose their actual flow paths. Finally, as we leave the flow and observe its contact with the country rock, **David Minton** will discuss the intricate patterns formed along the margins of such lava flows and what they tell us about lava flows on the other planets. Following the presentations of this Fabulous Four, return to camp and prepare to depart.

10:30 AM Depart the Valley of Fires campground and continue West on Route 380. This path takes us right by the exit for the Trinity site (unfortunately closed, and I could not arrange a special visit due to a "mission" that will engage the staff at White Sands Missile Range this weekend).

12:00 PM Stop for lunch near the small town of San Antonio

12:45 PM Enter I-25 and proceed South towards Las Cruces. At Hatch, exit onto the small Route 26 and travel West toward Deming (this is widely known as the "Hatch Cutoff". Beware of high-speed oncoming traffic on this small road). From Deming, take I-10 West toward Tucson

6:00 PM Arrive Tucson, unload vehicles, go home.

==Finis==

Drivers:

Primary: Dundas, Minton, Neish, Philippoff

Leaders: Jay Melosh, Adam Showman

Participants:

Archer, Doug
Bland, Mike
Choi, David
Diniega, Serina
Dundas, Colin
Fan, Guo
Minton, David
Neish, Catherine
Ong, Lissa
Palmer, Eric
Philippoff, Andrea
Schad, Tom
Schrader, Devin
Van Auken, Robin
Volk, Kat

Field Guide Editor: Colin Dundas

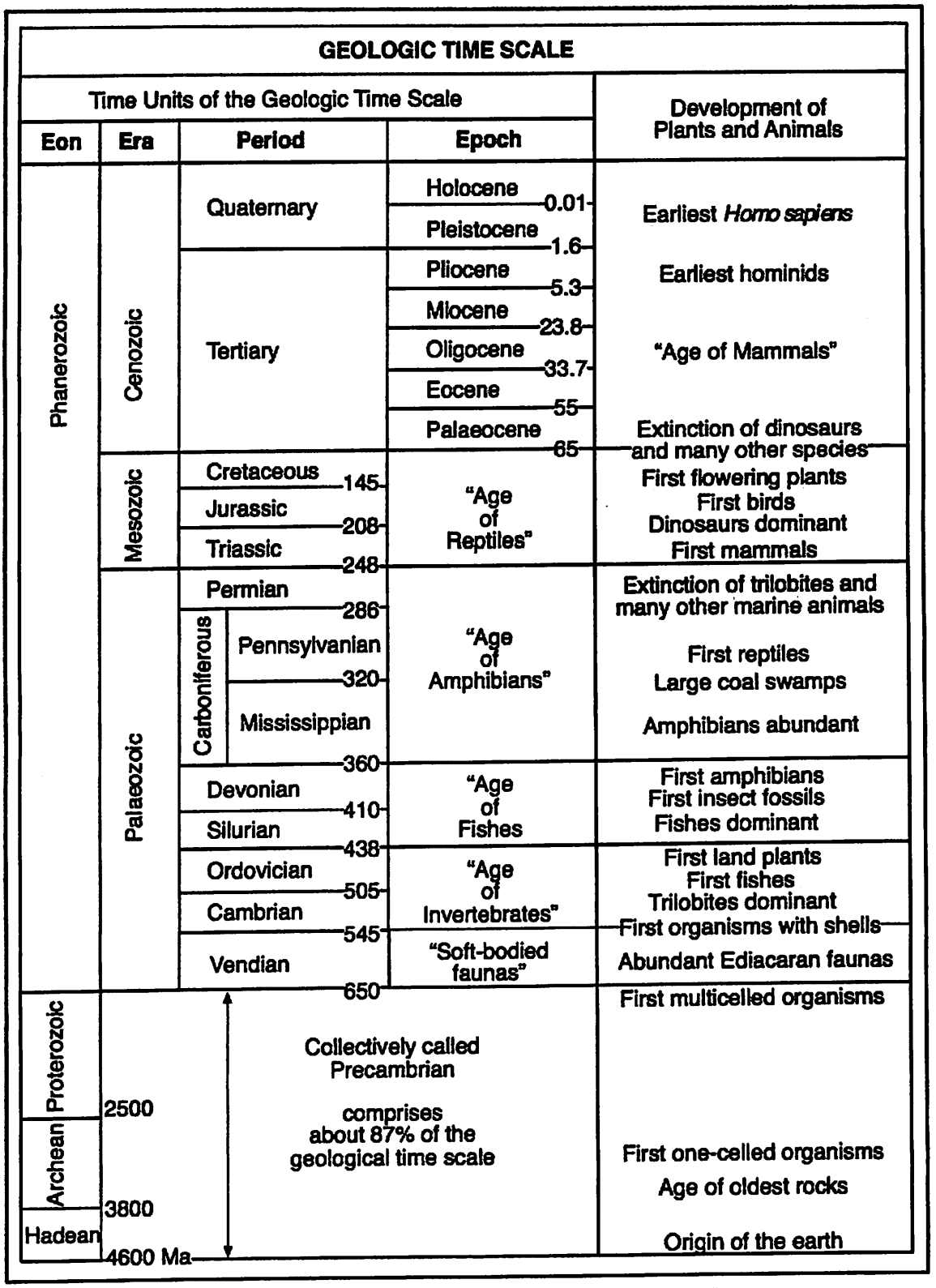

(From http://sci.waikato.ac.nz/evolution/geological.shtml)

Fault types

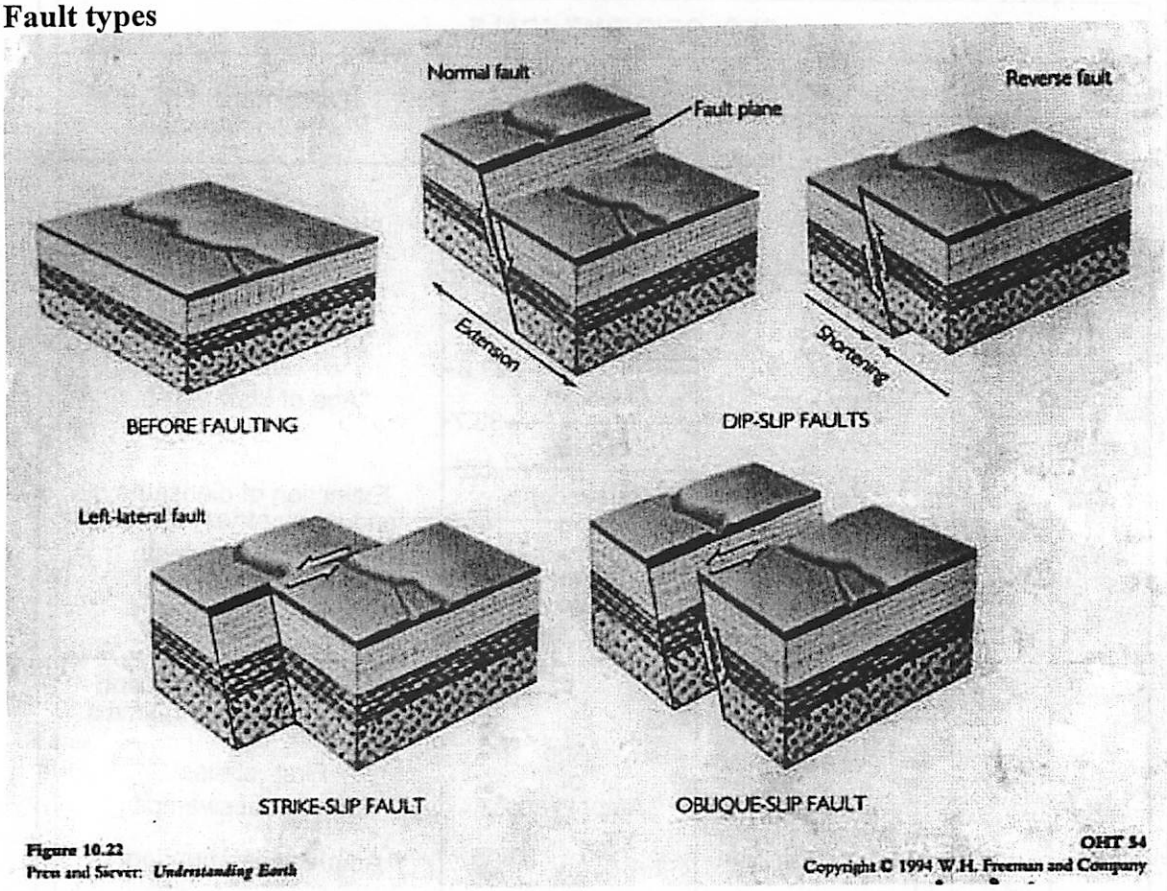

Figure 10.22
Press and Siever: *Understanding Earth*

OHT 54

Udden-Wentworth Grain Size Scale

Size Range	Name
>256 mm	Boulder
64-256 mm	Cobble
4-64 mm	Pebble (occasionally subdivided)
2-4 mm	Granule
1-2 mm	Very Coarse Sand
0.5-1 mm	Coarse Sand
0.25-0.5 mm	Medium Sand
125-250 μm	Fine Sand
62.5-125 μm	Very Fine Sand
31.25-62.5 μm	Silt
15.75-31.25 μm	Clay

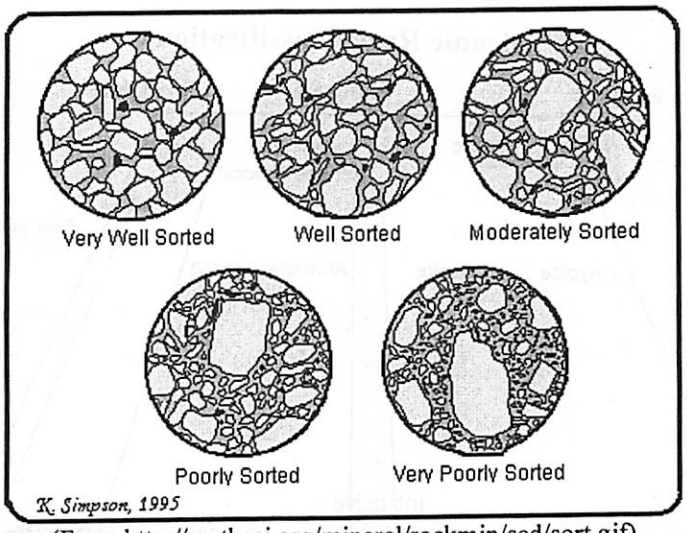

(From http://earthsci.org/mineral/rockmin/sed/sort.gif)

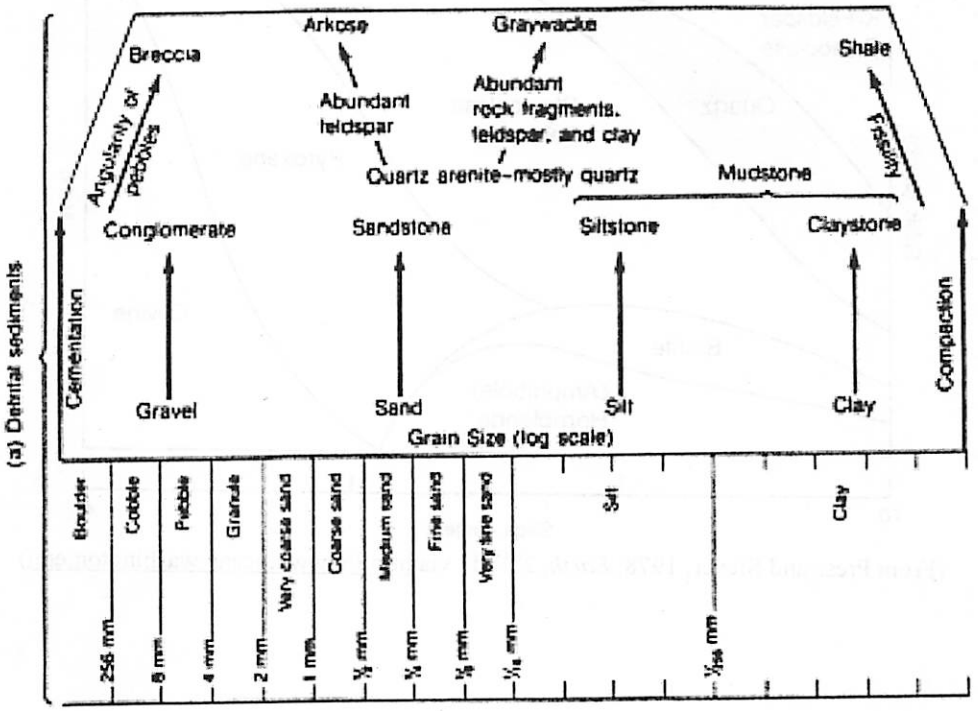

(b) Chemical sediments

Rock	Limestone	Dolomite	Iron formation	Evaporite	Chert	Organics	Phosphate
Chemical composition	$CaCO_3$	$CaMg(CO_3)_2$	Fe-silicate -oxide carbonate	NaCl $CaSO_4$	SiO_2	Carbon	$Ca_3(PO_4)_2$
Minerals	Calcite (Aragonite)	Dolomite	Hematite Limonite Siderite	Gypsum Anhydrite Halite Other salts	Opal Chalcedony Quartz	Coal Oil Gas	Apatite

Figure 3-22
Sedimentary rock classification. (a) Detrital sediments, (b) Chemical sediments.

(From http://www2.ocean.washington.edu)

Volcanic Rock Classification

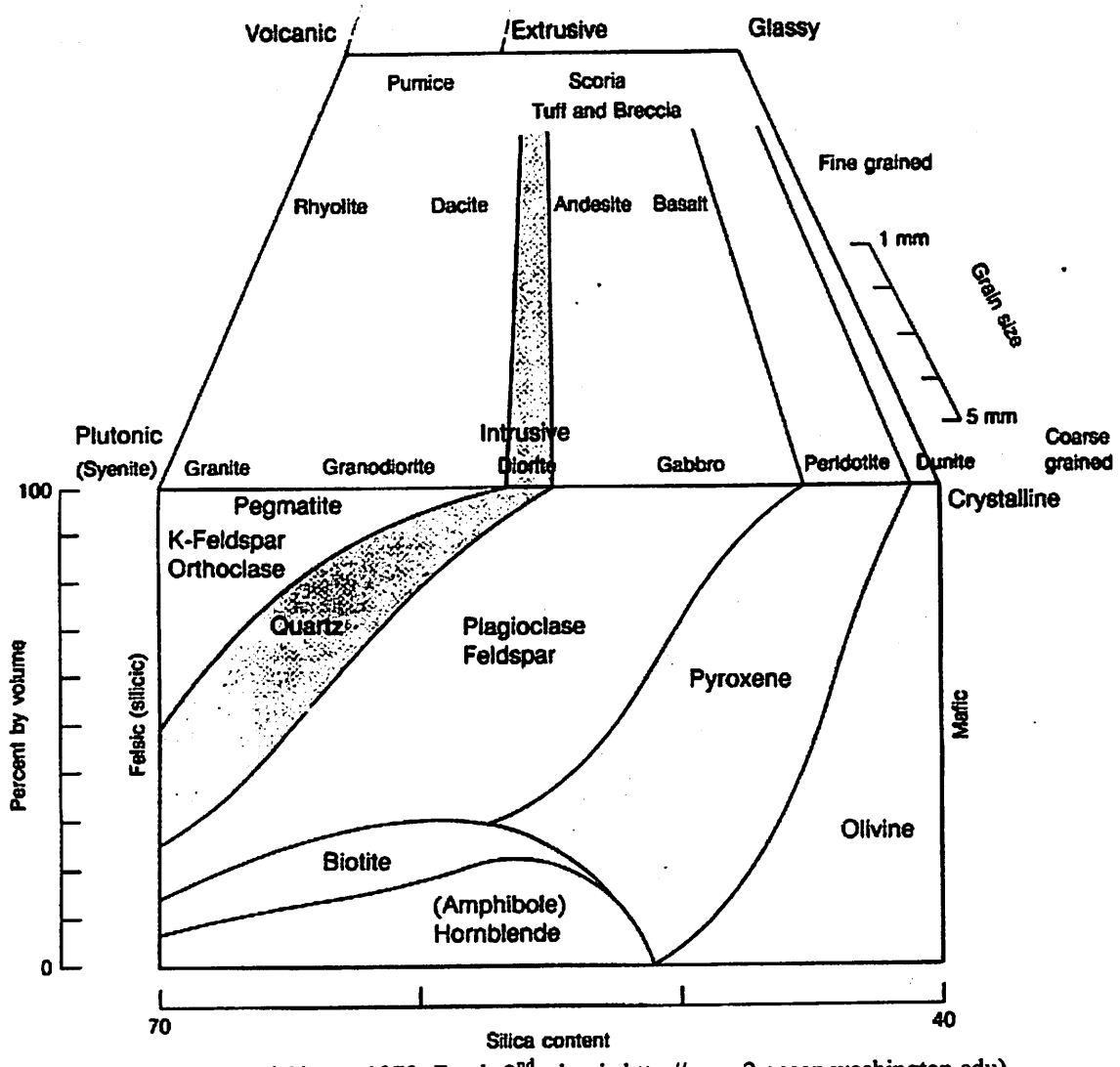

(From Press and Siever, 1978, *Earth*, 2nd ed., via http://www2.ocean.washington.edu)

Sand Dune Types

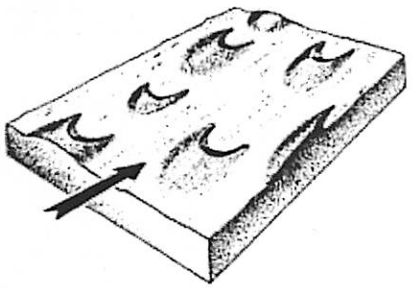

BARCHAN DUNES. Arrow shows prevaining wind direction.

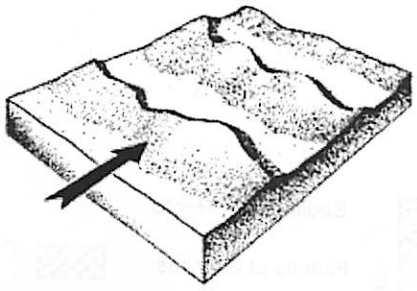

BARCHANOID RIDGE. Arrow shows prevaining wind direction.

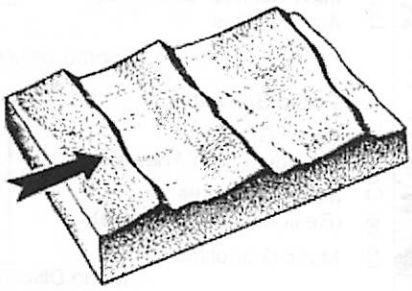

TRANSVERSE DUNE. Arrow shows peevaining wind direction.

Figure 3. From McKee, 1979

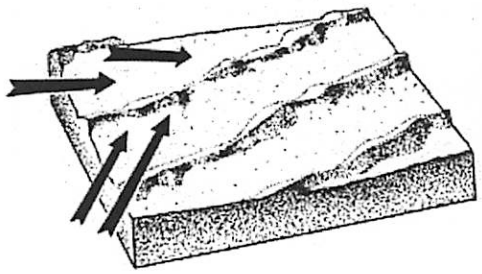

LINEAR DUNES. Arrows show probable dominant winds.

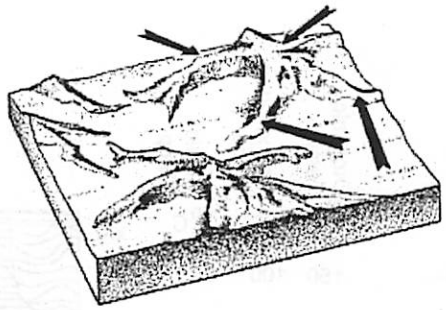

STAR DUNES. Arrows show effective wind directions.

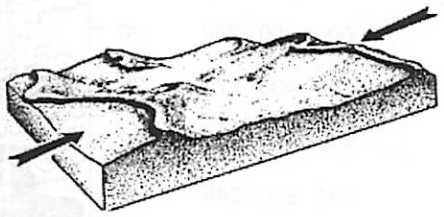

REVERSING DUNES. Arrows show wind directions.

Figure 4. From McKee, 1979

(From McKee, USGS Professional Paper 1052, via http://digital-desert.com/natural-formations/sand-dunes.html)

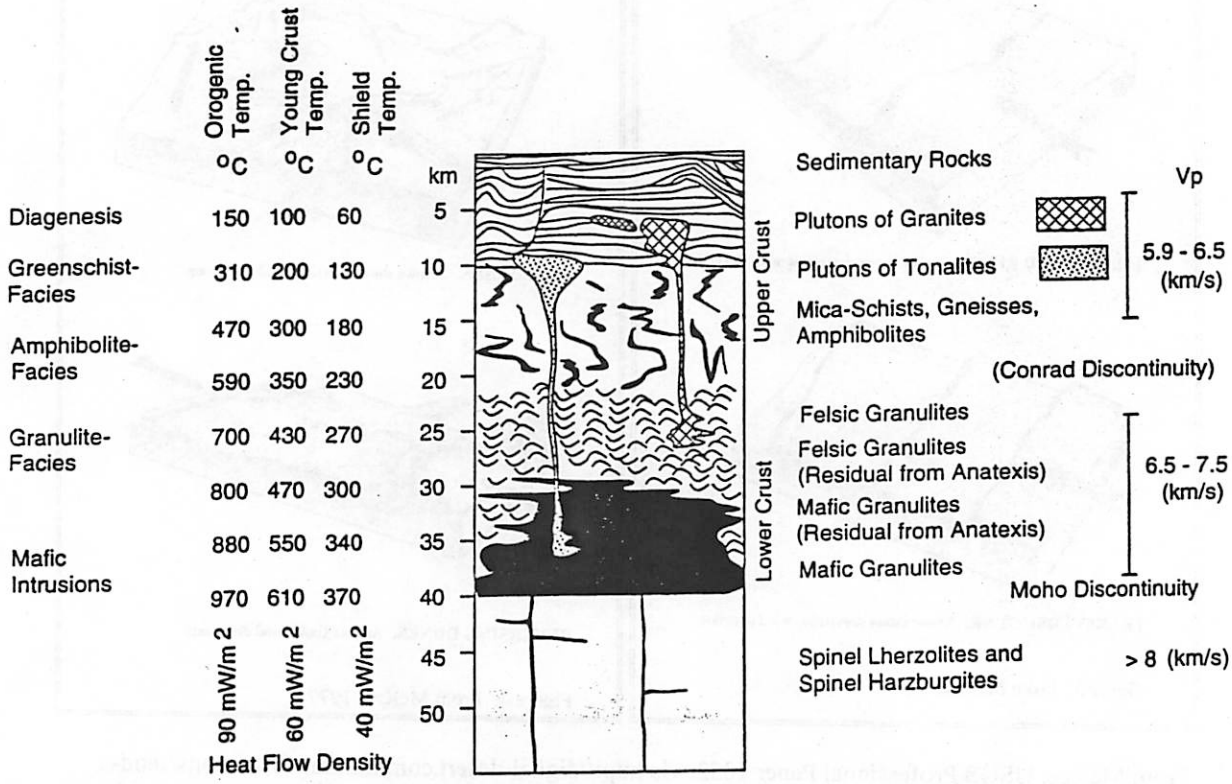

FIG. 9. Cartoon of the standard profile of the continental crust with temperature-depth relations of 3 geotherms calculated by Chapman (1986).

Wedepohl (1995)

Generalized Geologic Map of New Mexico

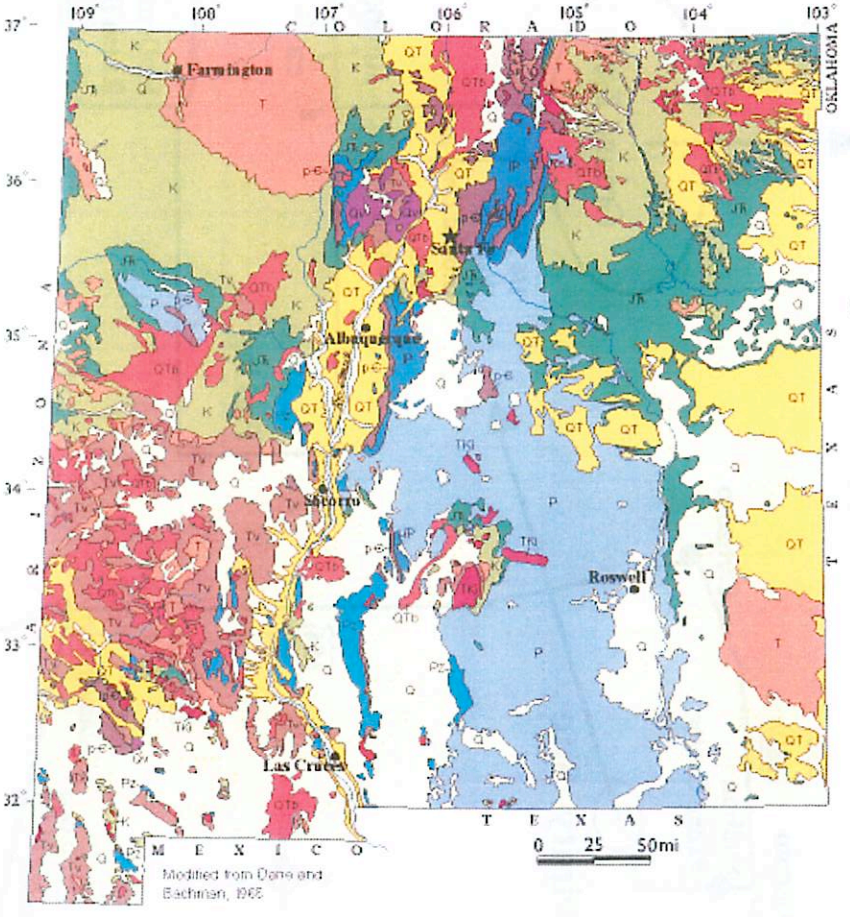

EXPLANATION

ERA	PERIOD	SEDIMENTARY	IGNEOUS
CENOZOIC 65 m.y.-present	QUATERNARY	Q	Qv
	TERTIARY	QT, T	QTb, Tv, Ti
MESOZOIC 245 m.y.-65 m.y.	CRETACEOUS	K	
	JURASSIC	JR	
	TRIASSIC		
PALEOZOIC 544 m.y.-245 m.y.	PERMIAN	P	
	PENNSYLVANIAN	IP	
	MISSISSIPPIAN	Pz	
	DEVONIAN		
	SILURIAN		
	ORDOVICIAN		
	CAMBRIAN		
PRECAMBRIAN 4.5 b.y.-544 m.y.		p€	

- Q — Quaternary sediments
- QT — Quaternary-Tertiary sediments
- Qv — Quaternary rhyolites and tuffs
- QTb — Quaternary-Tertiary basalts and andesites
- T — Tertiary sediments
- Tv — Tertiary volcanics
- Ti — Tertiary-Cretaceous intrusives
- K — Cretaceous sediments
- JR — Jurassic-Triassic
- P — Permian
- IP — Pennsylvanian
- Pz — Paleozoic undifferentiated
- p€ — Precambrian

Mileage Chart

San Antonio to Stallion exit	12
Carrizozo to Stallion exit	53
Highway 380 to Stallion	5
Stallion to Trinity Site	17
San Antonio to Socorro	10
San Antonio to Albuquerque	81
San Antonio to Las Cruces	130
San Antonio to El Paso	175
Carrizozo to Tularosa	46
Carrizozo to Alamogordo	56
Carrizozo to El Paso	146
Trinity Site to Alamogordo via the caravan	85

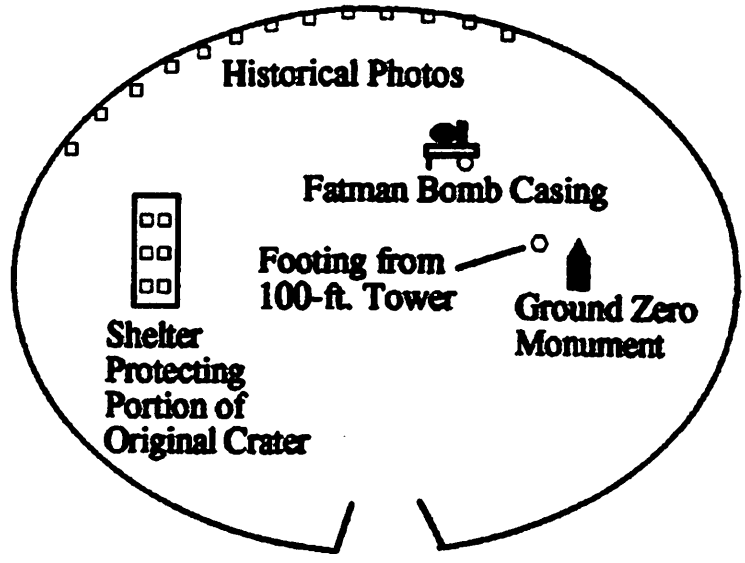

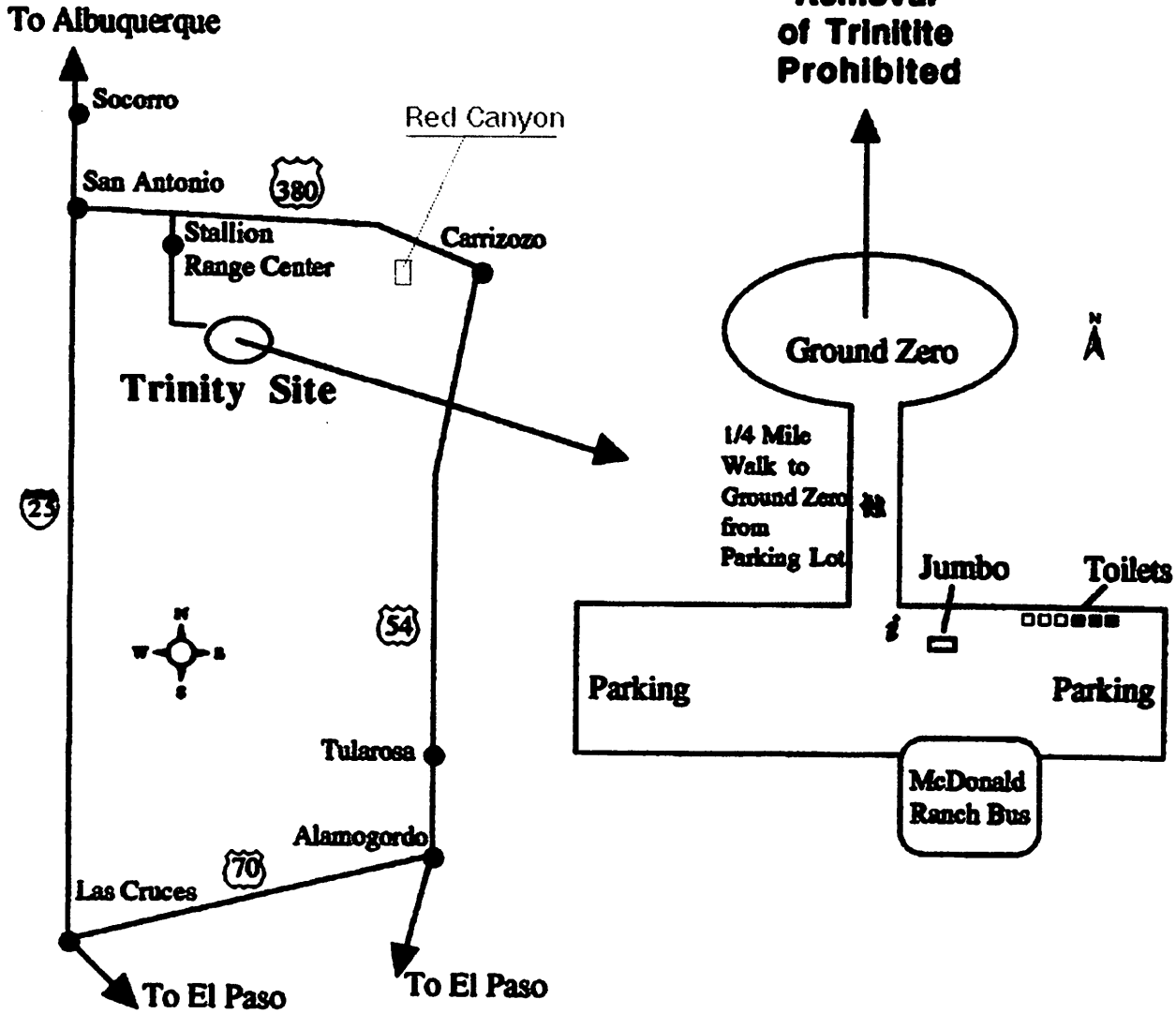

Spheroidal Weathering: Texas Canyon, Mars, Titan?

Presented by Tom Schad

Introduction

Geological weathering describes the breakdown, or initial erosion, of base rock material through mechanical and chemical processes. Usually rocks erode due to a combination of mechanical and chemical effects. Mechanical weathering, in contrast to chemical weathering, maintains the original composition of the base rock material. Examples of such weathering include the cracking of rock due to frost wedging[1], the influence of plants and animals, as well as other natural phenomena. Chemical weathering decomposes rock material through the interaction of the rock material with a decomposing agent. On Earth, the decomposing agent is usually a weak carbonic acid formed by falling rain and carbon dioxide.

Spheroidal Weathering

Decay resulting in rounded formations, and often spherical exfoliation[2], is referred to as spheroidal weathering.[3] More generally, spheroidal weathering is the chemical decomposition of rock material such that decay occurs more rapidly along the edges and corners of rock leading to a rounded geometry. It is the geometry of this weathering that defines it as 'spheroidal,' and it is the chemical nature of this weathering that allows it to be spheroidal. As Figure 1 illustrates, the edges and corners of rocks decay more quickly due to a larger surface area to material ratio in those areas. Chemical rates of reaction increase with larger surface area.

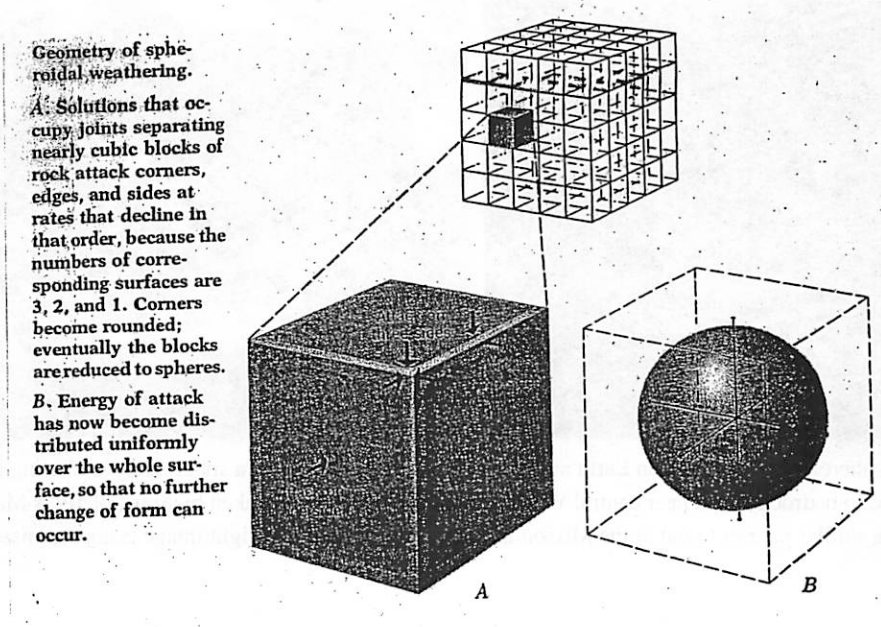

Fig. 1: The Geometry of Spheroidal Weathering (Courtesy of Flint &Skinner, 1977)

1 Frost wedging breaks apart rocks through the expansion of ice within existing cracks. As water freezes it expands resulting in a wedging effect within a rock capable of disintegrating the base rock.

2 Exfoliation is a specific type of mechanical weathering which erodes source material in layers.

3 Alternative names often associated with spheroidal weathering include spalling, onion-skin weathering, and concentric weathering; though, spalling and onion-skin weathering are better associated with general exfoliation. Spheroidal weathering is a more specific type of weathering.

Identification of Spheroidal Weathering: Texas Canyon

Spheroidal weathering, according to C.D. Ollier, must effect every side of the rock involved, including the bottom. In order to achieve pure spheroidal weathering, Ollier argues that rocks must be embedded below the surface. Once uncovered, one can identify it by its two main characteristics (See Figures 2-5):

(1) Uniform decomposition around a rounded boulder

(2) Exfoliation, or color banding, in concentric layers

In general, hard, homogeneous rocks, such as granite, dolerite and basalt, are more likely to exhibit this type of weathering. Texas Canyon, in Southeast Arizona, hosts a bounty of granite boulders that would be ideal prospects for spheroidal weathering.

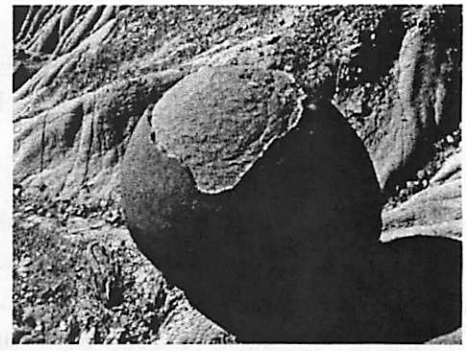

Fig. 2: Resulting from spheroidal weathering, a rounded boulder exfoliates concentric layers of material.

Spheroidal Weathering on Mars and Titan

Some evidence for spheroidal weathering on the surface of Mars has been achieved by the Spirit Rover of JPL's Mars Exploration Rover Mission (See Figure 3). Considering chemical weathering on Earth requires water and carbon dioxide to form a weak carbonic acid as a decomposing agent, this might suggest a similar process on Mars, at least at one time, and thus make a case for the presence for liquid water on Mars. Titan, being another hard surface body with available water, might also be a good place to search for spheroidal weathering.

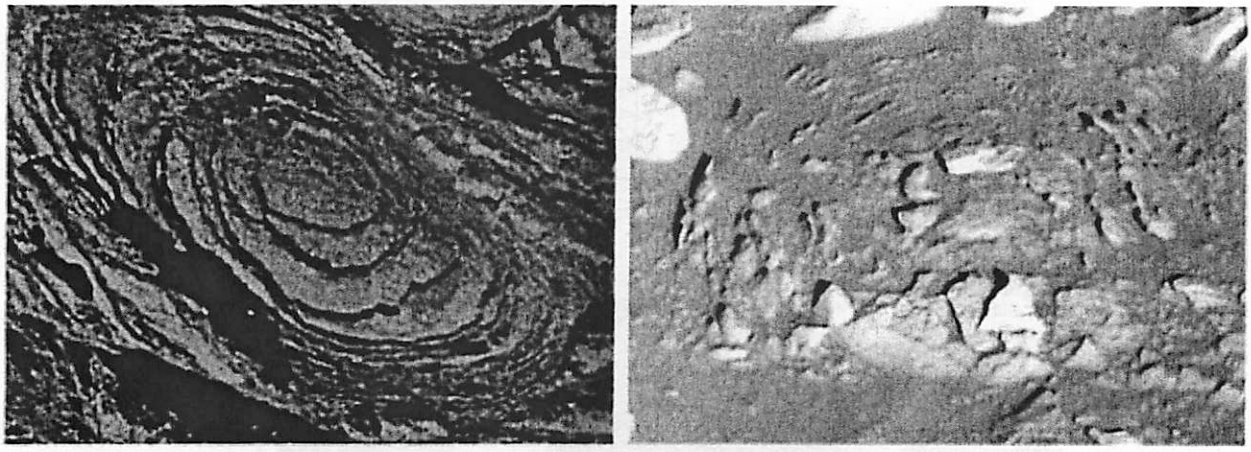

Fig. 3: Comparison of spheroidal weathering on Earth and Mars. The left image shows a spheroidal weathering pattern on a basaltic rock submerged in bedrock found near central Washington. The right image, taken by Spirit of JPL's Mars Exploration Rover Mission, shows a similar pattern found in the Missoula Crater. The scale of the right image is approximately 25 cm.

References:

Flint, R.F. & Skinner, B.J. Physical Geology. 2nd Ed. Wiley: New York, 1977.

Ollier, C.D. "Causes of Spheroidal Weathering." *Earth-Sci. Rev.,* 1971. V 7. 127-141.

Sarracino, R.S., Prasad, G., & Hoohlo, M. "A Mathematical Model of Spheroidal Weathering." *Mathematical Geology.* 1987. V. 19, No. 4, 269-289.

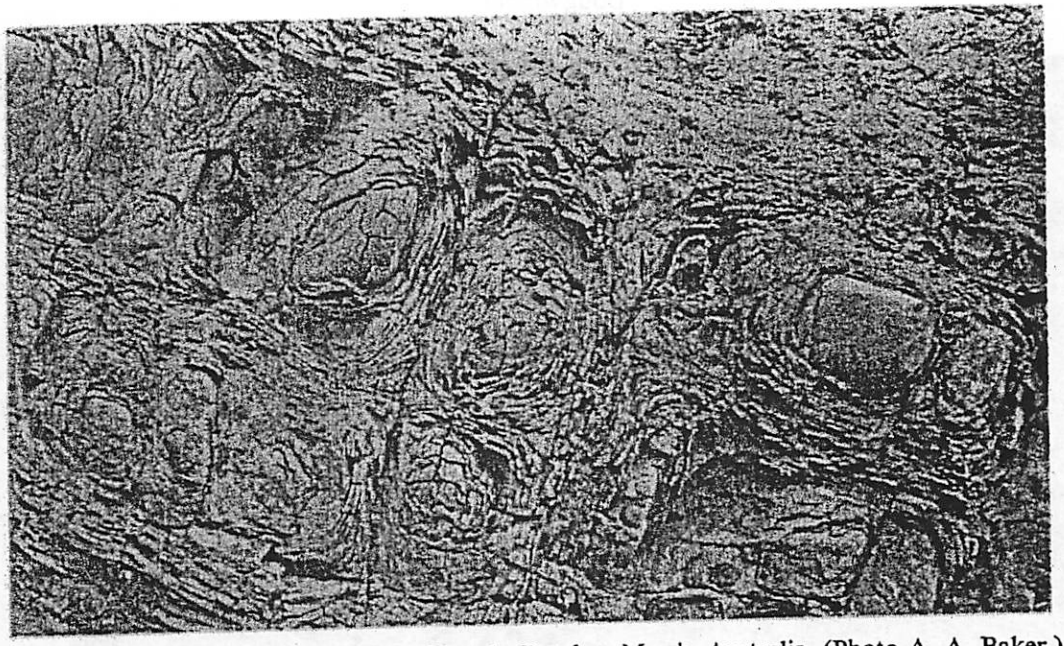

Fig. 4 Spheroidal weathering of basalt, Bacchus Marsh, Australia. (Photo A. A. Baker.)

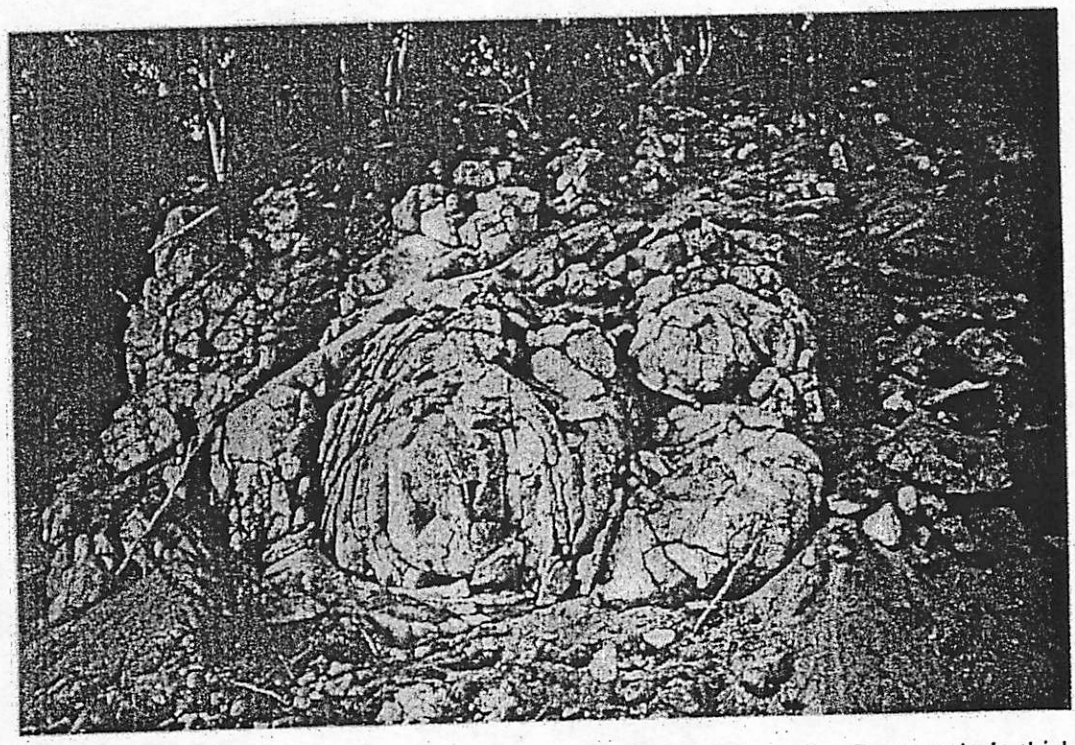

Fig. 5 Spheroidal weathering of granite, Kosciusko area, Australia. Comparatively thick shells have been formed. (Photo J. N. Jennings.)

Kilbourne Hole and other maar volcanoes from space

Doug Archer

Other Maar Volcanoes

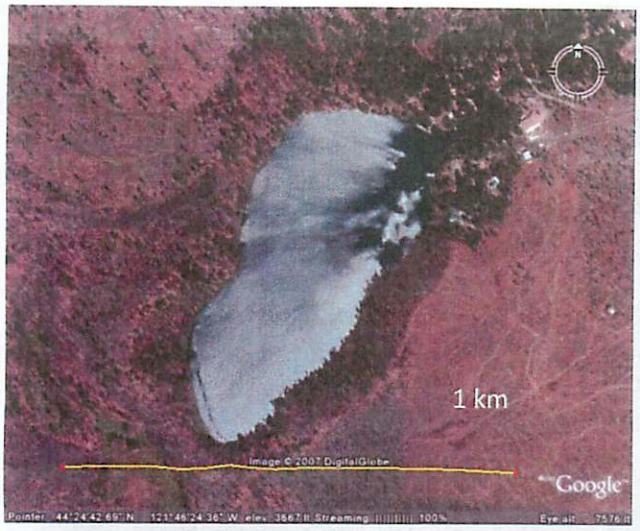

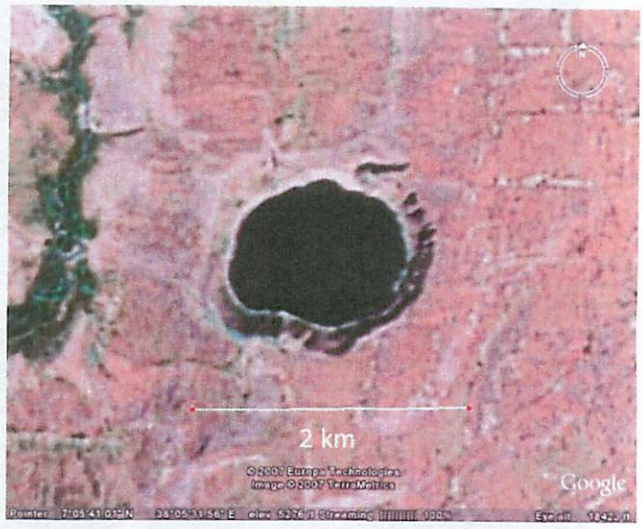

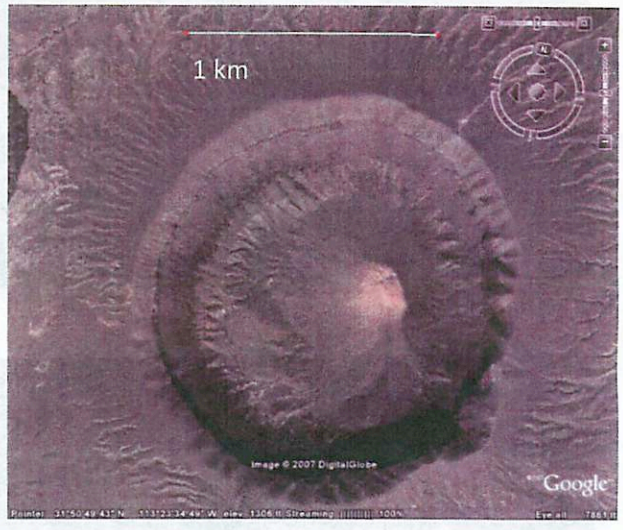

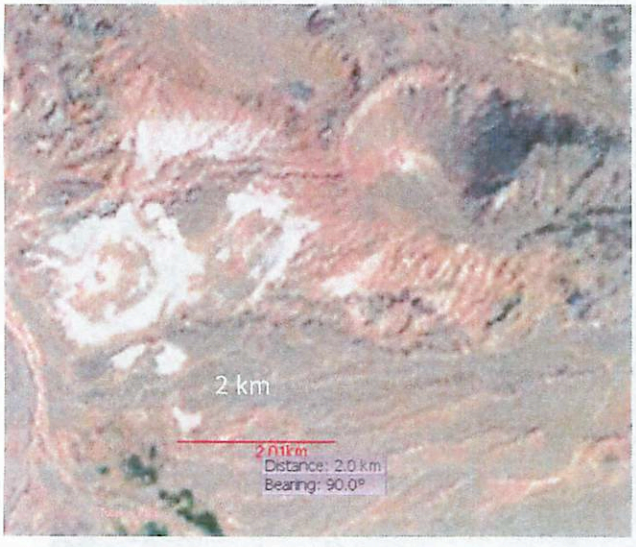

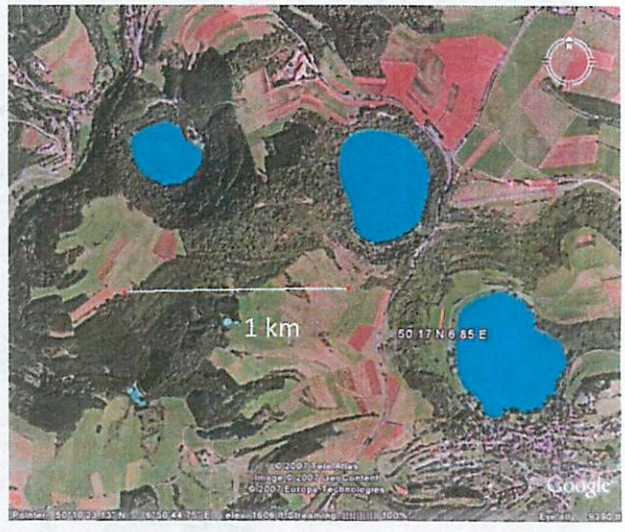

Find the Maar

Planetary Connection – Impacts vs. Maar Volcano Craters

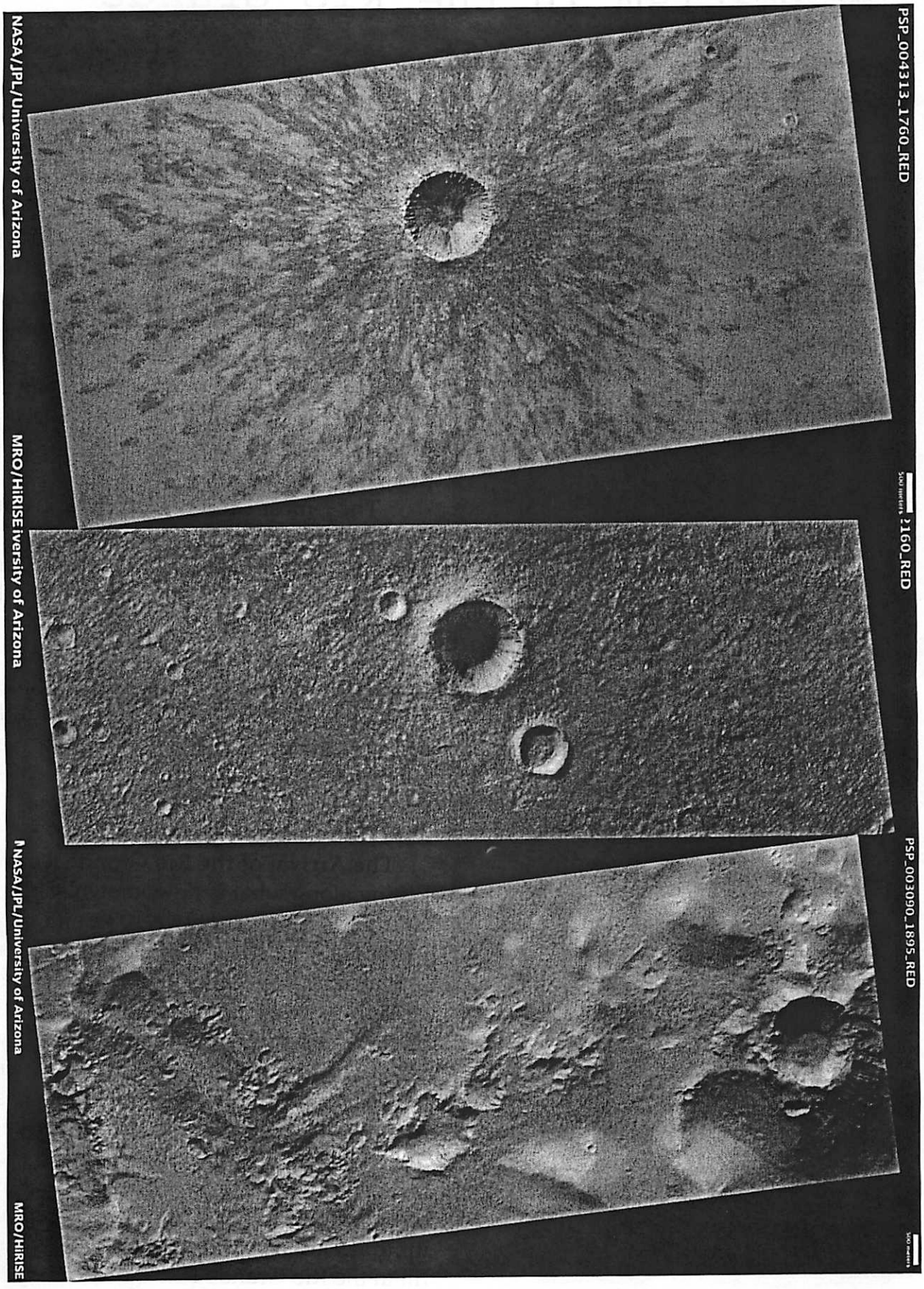

Magmatism in the Rio Grande Rift

Andrea Philippoff

rww.cliffshade.com/colorado/images/rgr.gif

BACKGROUND

Regional Overview

The Southwest is characterized by a complex geologic battle between compressional and tensional stresses. Orogenies have built mountain ranges and injected the crust with incredible volumes of magma, while continental rifting has stretched the lithosphere, in some places, to twice its original length (www.cliffshade.com...).

The most recent crustal crumble occurred between 72 and 40 Ma: the Laramide Orogeny. This event reactivated faults originally sliced to accommodate Proterozoic rifting, and supplied the magma that began mineralization along the Colorado Mineral Belt. After the close of the Orogeny, explosive volcanism riddled the southwest for several million years (www.cliffshade.com...).

RIFTING

The Arrival of the Rio Grande Rift

Rifting along what is now known as the Rio Grande Rift began between 32 and 27 Ma when a pull of regional extension capitalized on a north-trending zone of crustal weakness left by late Cretaceous/early Tertiary orogenies. By 26 Ma the developing rift had sufficiently pulled the crust apart to create a series of shallow basins that immediately began filling with beds of volcanic ash and basaltic lava flows, interspersed with alluvial sediment (Chapin, 1979) reaching depths of up to 7.3 km near Albuquerque, NM. Basin fill in the Rio Grande Rift is collectively

referred to as the Santa Fe Group and is characterized by coarse-grained sandstone interbedded with siltstone, conglomerate, and volcanic material that is generally soft and easily eroded (http://home.att.net/~sgeoveatch...).

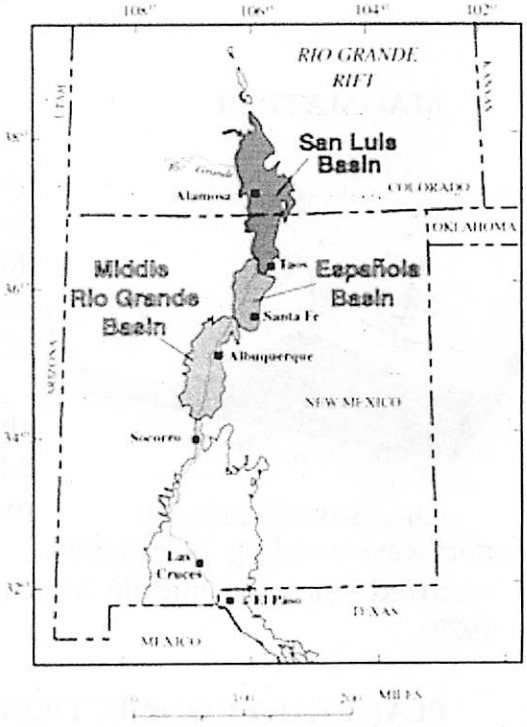

http://cires.colorado.edu/science/groups/sheehan/projects/riogrande/faq/

Extent

The Rio Grande Rift is a zone of crustal thinning caused by continental extension that is accompanied by unusually high heat flow and is often expressed in a series of asymmetric grabens and half-grabens. It spans a distance well over 1,000 km (Wells and Menges, 1987) north from the state of Chihuahua, Mexico (http://cires.colorado.edu...) to possibly as far as the southern edge of Wyoming, though Leadville, Colorado marks the northernmost surface expression of the Rift (www.cliffshade.com...). The three main basins identified in the rift zone include (from south to north) the Middle Rio Grande Basin, the Espanola Basin, and the San Luis Basin (http://cires.colorado.edu...).

Mechanism

The leading hypothesis for Rio Grande rifting invokes a pure-sheer, symmetrical model in which the lower crust (~20 miles down) has been extended four times the length of that of the upper crust (www.nmsu.edu...). Rifting continues today at a rate of approximate 5 mm/year (http://cires.colorado.edu) .

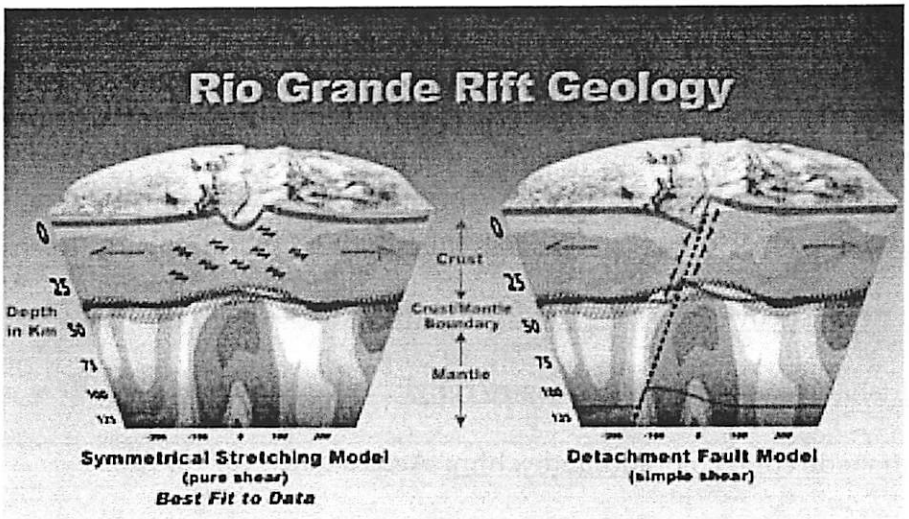

http://www.nsf.gov/news/mmg/mmg_disp.cfm?med_id=54361&from=mn

MAGMATISM

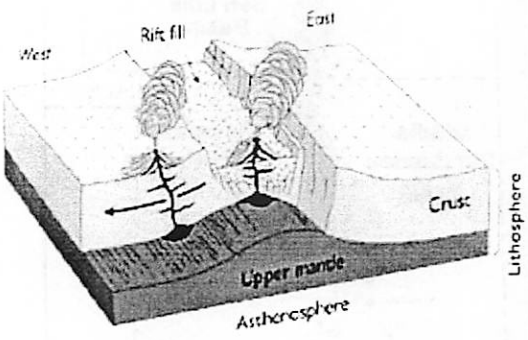

http://cires.colorado.edu...

As the Rio Grande Rift began to pull the North American plate apart, a series of en echelon tears developed into lineaments in the basement rock beneath the southern Rocky Mountains. These lineaments act as conduits of magma, high levels of heat flow, and geothermal activity (Chapin, 1979).

After a mid-Miocene lull (~20-13 Ma), volcanism along the Rio Grande Rift became increasingly robust. The Jemez Mountains and Socorro area received a high proportion of the magmatism at this time, due to their location above major northeast-trending lineaments. Approximately 1100 meters of uplift around the rift have occurred since the middle Miocene, much of it taking place between 7 and 4 Ma (Chapin, 1979).

PLANETARY CONNECTION

Tensional forces of sufficient strength resulting from any number of causes (such as plate tectonics or volcanism) acting on the surface of a body in space can act to rip the outer layer of that body apart. The scars from this strain will always manifest themselves in the form of normal faults, often in the form of grabens or half-grabens. Evidence for extension has been well documented on Mars (i.e. the Valles Marineris) and Venus, as well as Earth.

References:

Chapin, C.E. 1979. Evolution of the Rio Grande rift - A summary, In *Rio Grande Rift: Tectonics and Magmatism, R.E. Riecker, Editor.* American Geophysical Union. Washington, D.C.

Wells, S.G, and Menges, C.M. 1987. Geologic overview of north-central New Mexico and the 1987 Rocky Mountain cell-FOP fieldtrip route, In *Quaternary Tectonics, Landform Evolution, Soil Chronologies and Glacial Deposits-Northern Rio Grande Rift of New Mexico, field trip guidebook.* University of New Mexico.

http://cires.colorado.edu/science/groups/sheehan/projects/riogrande/faq/. Access date: 10/13/07.

http://home.att.net/~sgeoveatch/rio_grande_rift.htm. Access date: 10/13/07.

http://www.cliffshade.com/colorado/images/rgr.gif. Access date: 10/13/07.

http://www.cliffshade.com/colorado/index.htm. Access date: 10/13/07.

http://www.cliffshade.com/colorado/geo_overview.htm. Access date: 10/13/07.

http://www.nmsu.edu/~ucomm/Releases/2005/February/rio_grande_rift.html. Access date: 10/13/07.

http://www.nsf.gov/news/mmg/mmg_disp.cfm?med_id=54361&from=mn. Access date: 10/13/07.

White Sands Field Trip 2007
Mineralogy of the Crust and Mantle
Eric E. Palmer

Major Igneous Rock Forming Minerals

Pyroxene

Orthopyroxene

- Enstatite ($MgSiO_3$)
- Ferrosilite ($FeSiO_3$)

Clinopyroxene

- Diopside ($CaMgSi_2O_6$)
- Hedenbergite ($CaFeSi_2O_6$)
- Augite ($Ca_xMg_yFe_zSi_2O_6$)

Olivine (Perioditite)

- Fayalite (Fe_2SiO_4)
- Forsterite (Mg_2SiO_4)

Feldspar

- Plagioclase
  - Albite ($NaAlSi_3O_8$)
  - Anorthite ($CaAl_2Si_2O_8$)
- Alkali feldspars (K-Spar, Orthoclase)

Garnet $A_3B_2(SiO_4)_3$

- A&B can be: Mg, Fe, Mn, Ca, Al

Spinel ($MgSl_2O_4$)

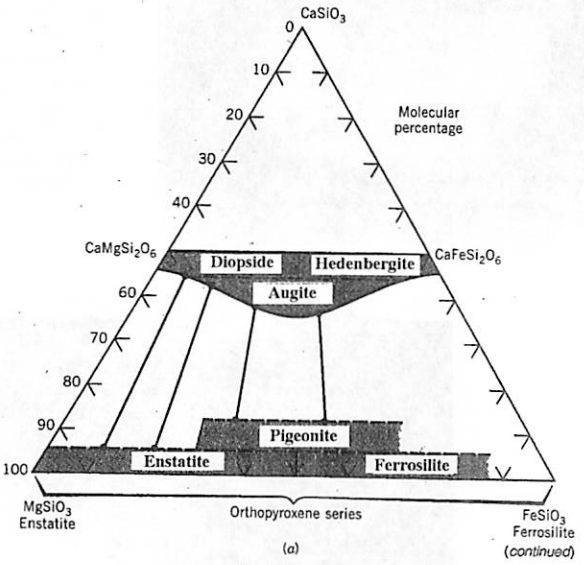

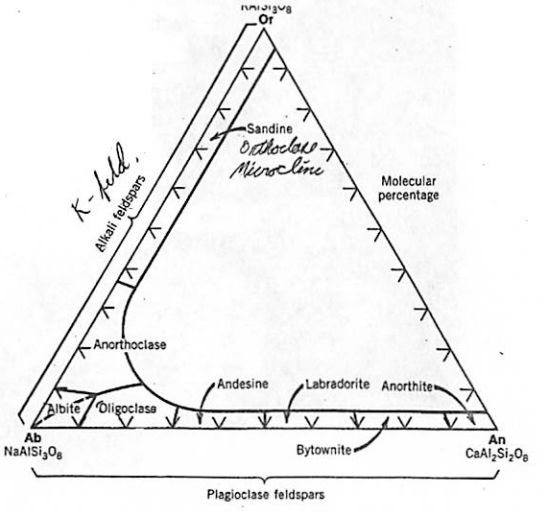

Composition of lherzolites

Mineral	Spinel	Garnet
Olivine	67%	63%
Orthopyroxene	24%	25%
Clinopyroxene	8%	2%
Spinel	2%	-
Garnet	-	10%

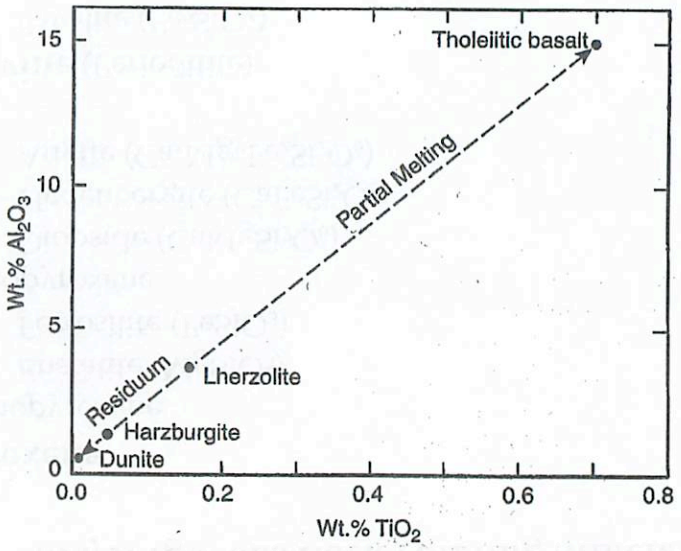

Figure 10–1 Relationship between TiO_2 and Al_2O_3 for garnet lherzolite, harzburgite, and dunite, as well as tholeiitic basalt, showing how the extraction of a basaltic partial melt from a garnet lherzolite can result in the creation of a solid refractory harzburgite or dunite residue. From Brown and Mussett (1993). Copyright © by permission Kluwer Academic Publishers.

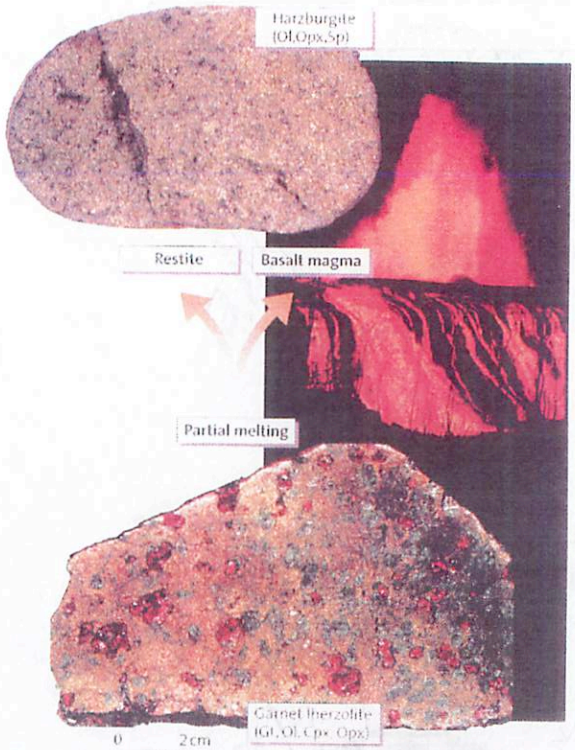

Fig. 3.12. Partial melting of mantle rock (garnet lherzolite) generates basaltic magma erupted in lava fountains at Kilauea volcano (Hawaii). Crystalline residue (restite) represented by xenoliths (olivine nodules) found in volcanoes (306). Photo of lherzolite rock slab from (438).

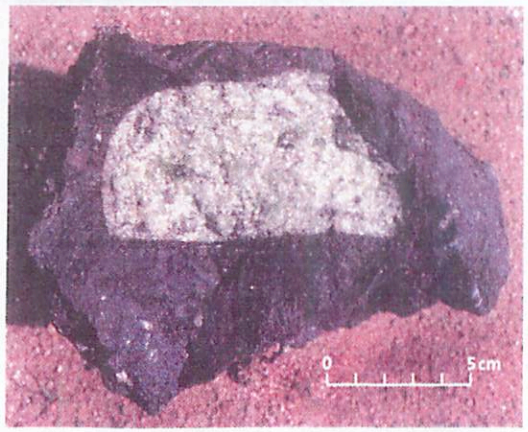

Fig. 3.5. Olivine nodule (harzburgite) from the phreatomagmatic deposits of the Late Quaternary Dreiser Weiher maar (Eifel, Germany). The light-green crystals are olivine, the dark-green pyroxene and the black crystals chromium spinel

Using silicon to determine general rock type

Rock Type	SiO_2 Content	
Picro-basalt	41 - 45	Ultra-mafic
Basalt	45 - 52	Mafic
Basaltic andesite	52 - 57	
Andesite	57 - 63	
Dacite	63 - 70	
Rhyolite	70 +	Felsic

Lherzolite

an ultramafic (little SiO_2) found in the mantle. It contains olivine and orthopyroxene with some aluminum spinals and garnets. It can have plagioclase at low pressure, but the plagioclase will be converted to spinel at depth (20-30 km). The spinel will become pyrope garnet below 90 km. Lherzolites can be partially melted to make basalt. The residual rock is called a Harzburgite, or if there is more melting, a Dunite, which is almost totally olivine.

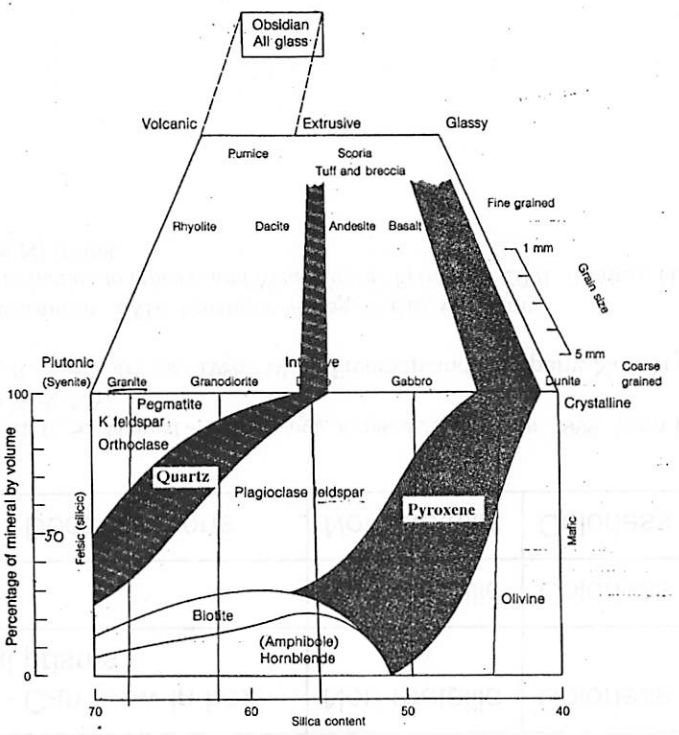

Mineral Name	Color	Hardness	Cleavage/Crystal	Luster	Streak
Pyroxene	White, Green, Black, Brown	5-6	Nearly 90 deg	Non-metallic	Colorless
Orthoclase (K-spar)	Colorless, white, gray, cream, red	6	Two directions, 90 deg	Non-metallic	Colorless
Plagioclase	Colorless, white, gray	6	Two directions, 90 deg. Some parallel striations	Non-metallic	Colorless
Quartz	Colorless, white, smoky, other	7	None - Can grow in hex-agonal prisms	Non-metallic	Colorless
Olivine	Grayish green, brown	6.5 - 7	None	Non-metallic	Colorless
Garnet	Brown to red	6.5 - 7.5	None - Dodechedrons	Non-metallic	Colorless

Table 3-4
Mohs Scale of Hardness

Mineral	Scale number	Common objects
Talc	1	
Gypsum	2	Fingernail
Calcite	3	Copper coin
Fluorite	4	
Apatite	5	Knife blade
Orthoclase	6	Window glass
Quartz	7	Steel file
Topaz	8	
Corundum	9	
Diamond	10	

References:

Klein, C. and Hurlbut, C. S. *Manual of Mineralogy, Revised 21st Edition* 1999. John Wiley and Sons, Inc, New York, NY.

Press, F. and Siever, R. *Earth, 4th Ed.* 1986. W. H. Freeman and Company, New York, NY

Schmincke, H. U. *Volcanism.* 2004. Springer-Verlag, Berlin, Germany

Winter, J. D., *An Introduction to Igneous and Metamorphic Petrology.* 2001. Prentice Hall, Upper Saddle River, NJ 07458.

Robert Goddard and the First Space Rockets

Kat Volk

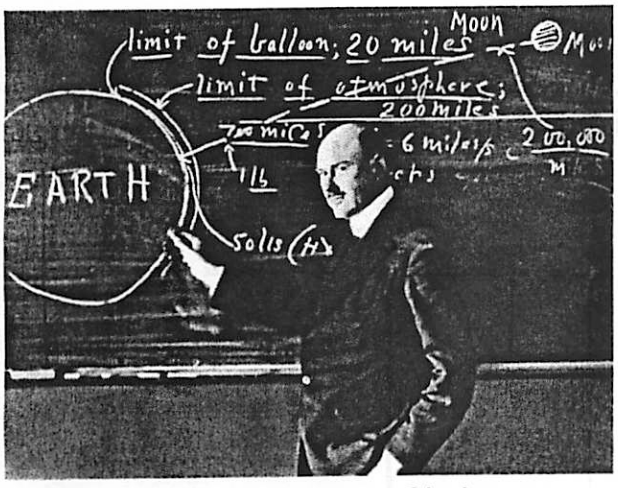

1924: Goddard lectures at Clark University in Massachusetts

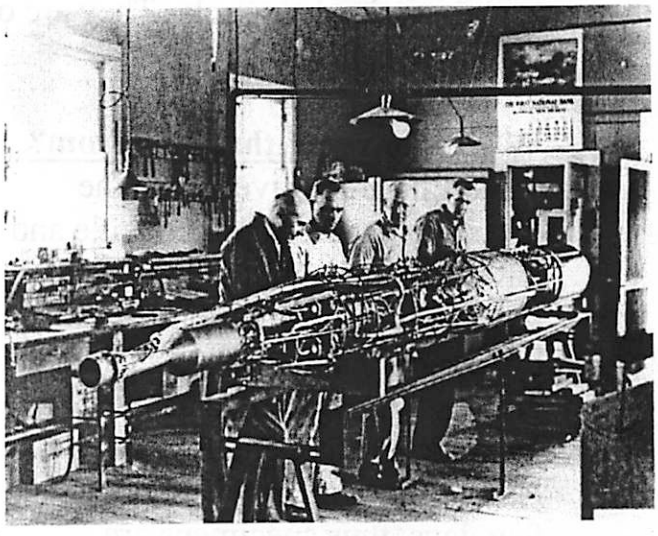

1940: At the rocket shop in Roswell, NM

(Very) Basic timeline of Goddard's contributions to rocketry:

- 1912: Considers the practical use of rocket propulsion
- 1915: Proves that rockets provide thrust in a vacuum
- 1926: Achieves first flight for liquid-fuel rocket
- 1929: First rocket flight with scientific payload
- 1932: First use of vanes and gyroscopes to stabilize rockets
- 1935: Liquid-fuel rocket exceeds the speed of sound.
- 1937: Altitude of 8000 ft reached.

Goddard at the controls for a launch

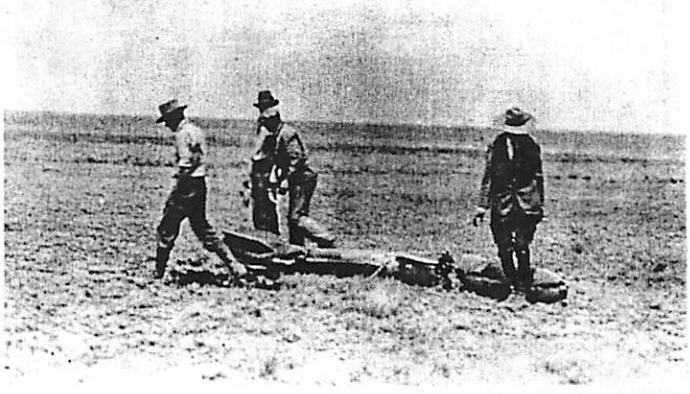

Test flight April 19, 1932

source for all images: grin.hq.nasa.gov

Xenoliths and Crustal Evolution at Kilbourne Hole: Not Just Pretty Rocks

Presented by: Mike Bland

What are Xenoliths? Xenoliths are inclusions or enclaves of preexisting rock in an igneous rock. They are often derived from the "country rock" (or wall rock).

Where do xenoliths come from?

Xenoliths are derived from the deep crust and/or upper mantle and have been brought to the surface during volcanic eruptions (usually by Maar volcanoes). As such they give us unprecedented access to the upper mantle and lower crust. Ascent times are a few hours to a few days, thus specimens are largely unaltered.

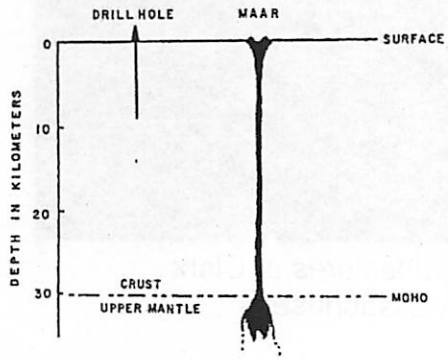

Fig 1: Comparison of depth of deepest drill holes to depth of xenoliths. From Padovani and Carter 1977.

A review of Maar volcanoes:

Maar volcanoes form from the interaction of ground water and rapidly ascending magma which creates an extremely energetic eruption.

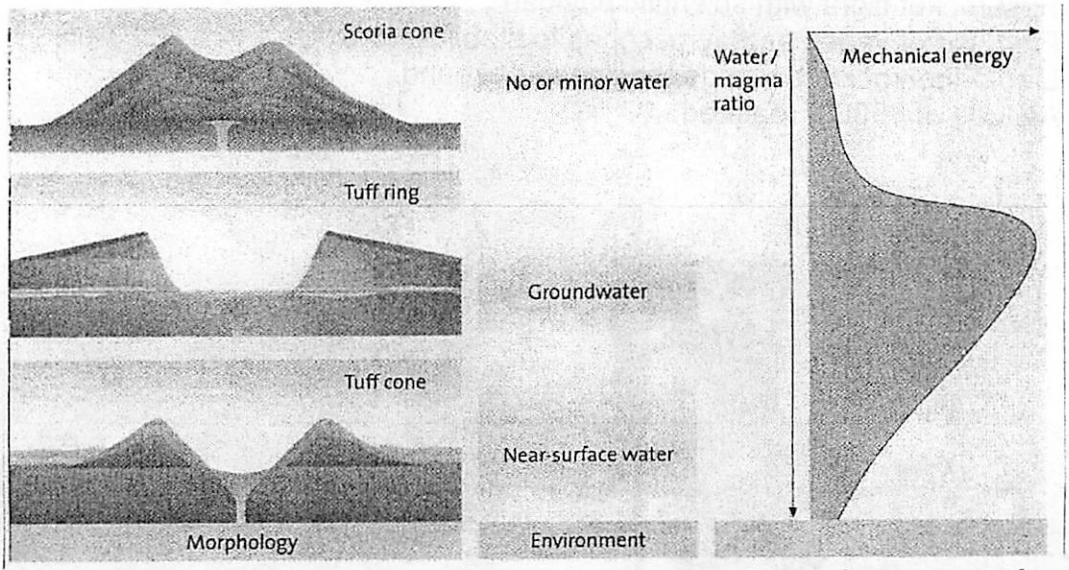

Fig 2: Mechanical energy of an eruption as a function of water content. Maar volcanoes are similar to tuff rings in morphology. From Schincke. Volcanism. 2004.

Kilbourne Hole:

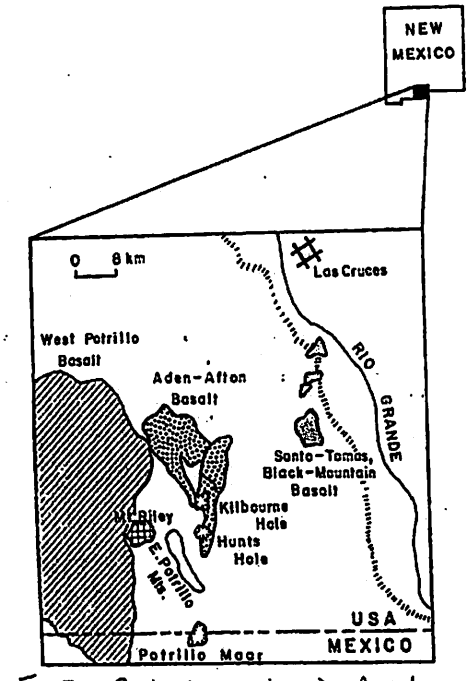

Fig 3: Potrillo volcanic field from Padovani + Carter 1977.

Kilbourne Hole is a Late Pleistocene (~80 kyr) maar in south central New Mexico, located within the southern Rio Grande Rift. The maar is part of the Potrillo volcanic field and measures 2.3 x 3.3 km.

Stratigraphy from bottom up
(courtesy of Pete Lanagan)
1. Camp Rice formation – mid Pleistocene sediments (lower half of crater)
2. Afton basalt – 5 m thick
3. Tuff ring ejected – upper half of crater wall
4. Holocene material – wind blown sand, etc.

Xenoliths at Kilbourne Hole:

Kilbourne hole contains xenoliths both from the lower crust and from the upper mantle (these are sometimes referred to as mantle nodules). The xenoliths are generally lherzolitic (ultramafic w/ 40-90% Olivine), and generally contain spinel ($MgAl_2O_4$), although some contain garnet ($Mg_3Al_2(SiO_4)_3$).

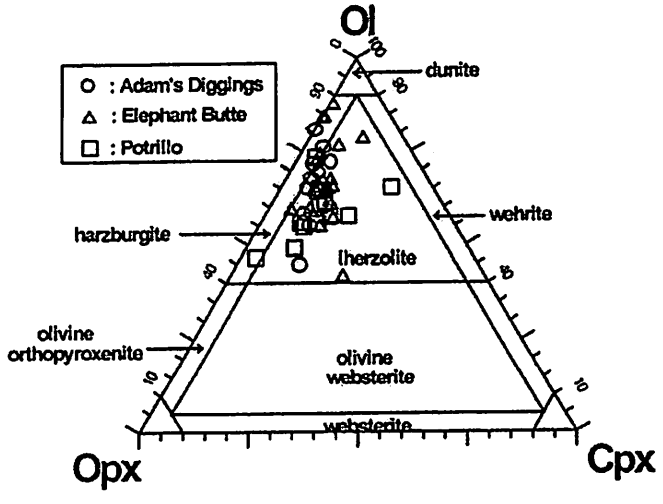

Fig. 4 Modal composition of spinel peridotites and harzburgites. *Ol* olivine, *Opx* orthopyroxene, and *Cpx* clinopyroxene

From Kil and Wendlandt 2004.

Geochemical analysis of xenoliths can tell us about both the pressure (depth) and temperature conditions from which the xenoliths. This provides constraints on the P-T-time conditions of the crust and upper mantle.

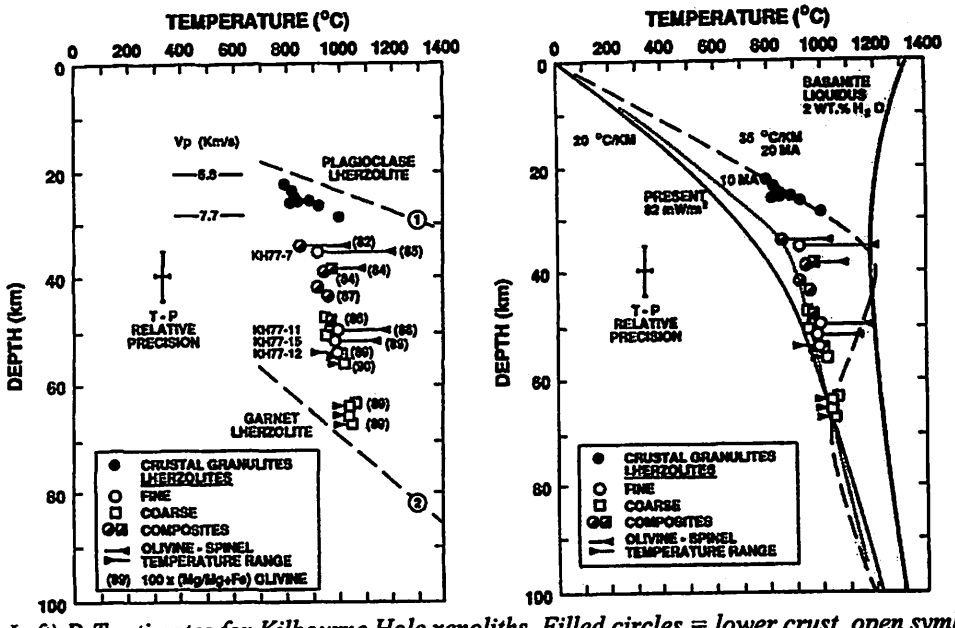

Fig.5 : Left) P-T estimates for Kilbourne Hole xenoliths. Filled circles = lower crust, open symbols = upper mantle. The lithosphere is well sampled at depths between 20 and 70 km. Right) Model geotherms at 20 Ma (dashed), 10 Ma (dotted), and present (solid). From Bussod and Williams 1991.

What do the xenoliths tell us about the crust/mantle at Kilbourne Hole?

Composition of the upper mantle

- Mantle xenoliths DO NOT represent primitive mantle
  - All have suffered one or more "depletion events"
  - Many lines of geochemical evidence point to significant partial melting of the upper mantle.
- The mantle consists of at least two components
  1. depleted MORB-like material
  2. enriched material (kimberlite)
- Kilbourne Hole xenoliths contain components of a Proterozoic (2.5 Ga – 550 Ma) crust AND Cenozoic basalt.
- Age of differentiation event is Mid to late Cenozoic – consistent with rift related volcanism.

Evolution of the Lithosphere

- Boundary between the lithosphere and asthenosphere greater than 42 km.

- Complex thermal history over the past 30 Ma.
    - Possible inversion of the thermal gradient of the upper mantle in the last 20 Ma.
    - Requires rapid transfer of heat directly to the crust-mantle boundary.
    - Likely regional crustal underplating by intrusion of magma into the lower crust (Pre-rifting).
- Lithospheric thinning commenced later then 12.6 Ma

The mantles of other planets:

We have a few samples of what appear to be pieces of mantle material from other planets:

- Mars: Nakhla is an ultramafic martian meteorite and so is "most" representative of the Martian mantle.
    - Upper mantle of Mars is lherzolitic (Olvine rich)
    - Richer in clinopyroxene and depleted in Al relative to Earth
- Vesta: Diogenites may represent mantle cumulates from the interior of Vesta
    - Olivine rich with significant Mg-orthopyroxenes

The compositions of terrestrial planet mantles appear to be broadly similar. However, the differences indicate important differences in crust/mantle processes.

Useful References:

Basaltic Volcanism Study Project, 1981. Basaltic volcanism on the terrestrial planets. Pergamon, New York, NY, 1286 pp.

Bussod, G.Y.A. and D.R. Williams, 1991. Thermal and kinematic model of the southern Rio Grande rift: inferences from crustal and mantle xenoliths from Kilbourne Hole, New Mexico. *Tectonophysics*, **197**, 373-389.

Cameron, K.L., J.V. Robinson, S. Niemeyer, G.J. Nimz, D.C. Kuentz, R.S. Harmon, S.R. Bohlen, and K.D. Collerson, 1992. Contrasting styles of Pre-Cenozoic and Mid-Tertiary crustal evolution in northern Mexico: Evidence from deep crustal xenoliths from La Olivina. *J. Geophys. Res.* **97**, 17353-17376.

Feigenson, M.D. 1986. Continental alkali basalts as mixtures of kimberlite and depleted mantle: evidence from Kilbourne Hole Maar, New Mexico. *Geo. Res. Lett.* **13**, 965-968.

Kil, Y. and R.F. Wendlandt, 2004. Pressure and temperature evolution of the upper mantle under the Rio Grande Rift. *Contirb. Mineral. Petrol.* **148**, 265-280.

Padovani, E.R. and J. Carter, 1977. Apects of deep crustal evolution beneath south central New Mexico. In: Heacock JG (ed), The Earth's crust: It's nature and physical properties, AGU Geophys. Monogr. **20**, 19-55.

Roden, M.F. A.J. Irving, V.R. Murthy, 1987. Isotopic and trace element composition of the upper mantle beneath a young continental rift: Results from Kilbourne Hole, New Mexico. *Geochemica et Cosmochimica Acta*, **52**, 461-473.

Scherer E.E., K.L. Cameron, C.M. Johnson, B.L. Beard, K.M. Barovich, K.D. Collerson, 1997. Lu-Hf geochronology applied to dating Cenozoic events affecting lower crustal xenoliths from Kilbourne Hole, New Mexico. *Chemical Geo.* **142**, 63-78.

Tectonics of the Rio Grande Rift

-Summary handout by Devin Schrader

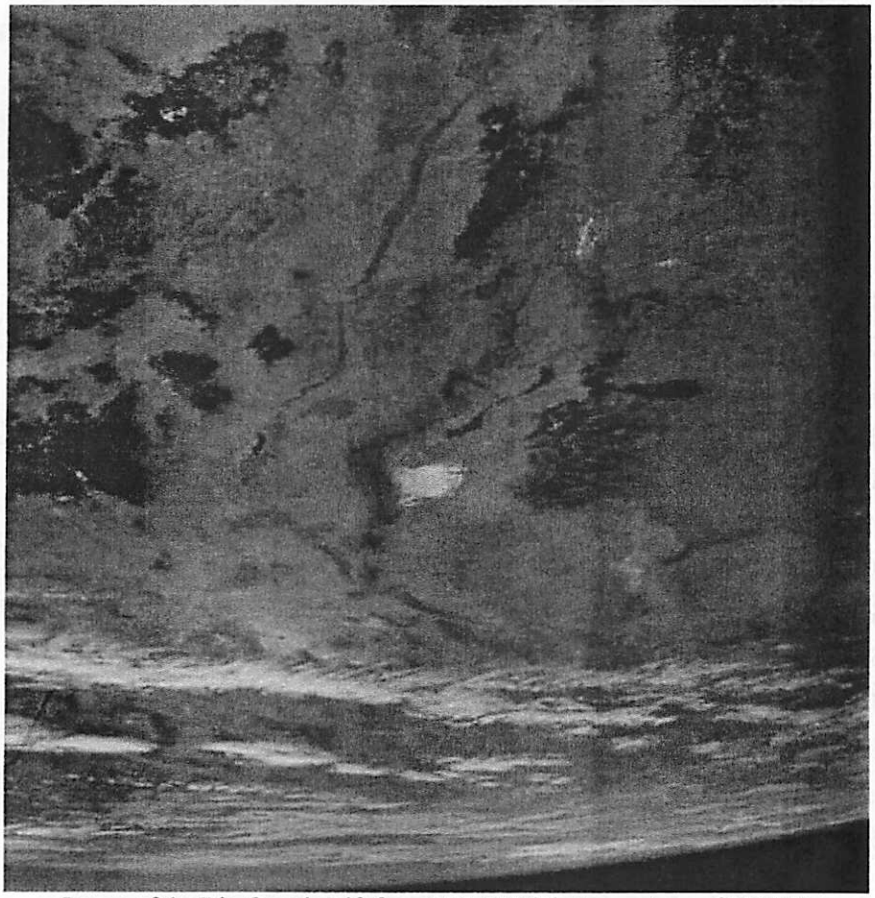

Image of the Rio Grande Rift from STS-100 (Photo courtesy of NASA)

The Rio Grande Rift spans more than 1000 km, from the Rocky Mountains in Leadville, Colorado, through New Mexico and west Texas, to Chihuahua, Mexico (Keller and Baldridge, 1999).

The rift's formation can be attributed to a "…transform boundary along which right-lateral slip…" occurred, due to "…plate-boundary forces acting along the western edge of the North American plate". Passively, the "…subduction of the Farallon plate beneath the North American plate…" caused initial extension of the rift. The result of the rift is a thinner region of the continental crust. Since the area the rift now encompasses had been previously uplifted compared to surrounding continental crust, gravitational collapse also played a role in rift formation (Keller and Baldridge, 1999).

"The Rio Grande rift region has certainly experienced considerable uplift since the Cretaceous…". This is supported because "…widespread Cretaceous marine shales and littoral sandstones indicate that this area was at or near sea level at this time…" (Keller and Baldridge, 1999).

There are two main eras of formation for the rift. Although, "*Chapin and Cather* (1994) pointed out that rifting has been to some degree continuous since its initiation at about 30 Ma…" (Keller and Baldridge, 1999). The rift began forming approximately at 30 Ma during the Oligocene (33.7 to 23.8 Ma) and lasted for ~10 Ma into the Miocene (23.8 to 5.3 Ma). The second major rifting event began approximately at 17 Ma and is ongoing (http://home.att.net/~sgeoveatch/rio_grande_rift.htm). Currently, the rift is relatively tectonically inactive compared to the past. Although, the largest rift-associated earthquakes were recorded only 101 years ago (each of magnitude ~5.8 were recorded in 1906 (http://en.wikipedia.org/wiki/Rio_Grande_Rift).

Forming events of the rift include "…Laramide (Late Cretaceous-Paleogene) compression or transpression, extensive Paleogene subduction-related volcanism, and finally extension. Basins in the rift commonly include a significant thickness of sediments deposited in the Laramide foreland-style basins, [and] mid-Tertiary volcanics…" (Keller and Baldridge, 1999).

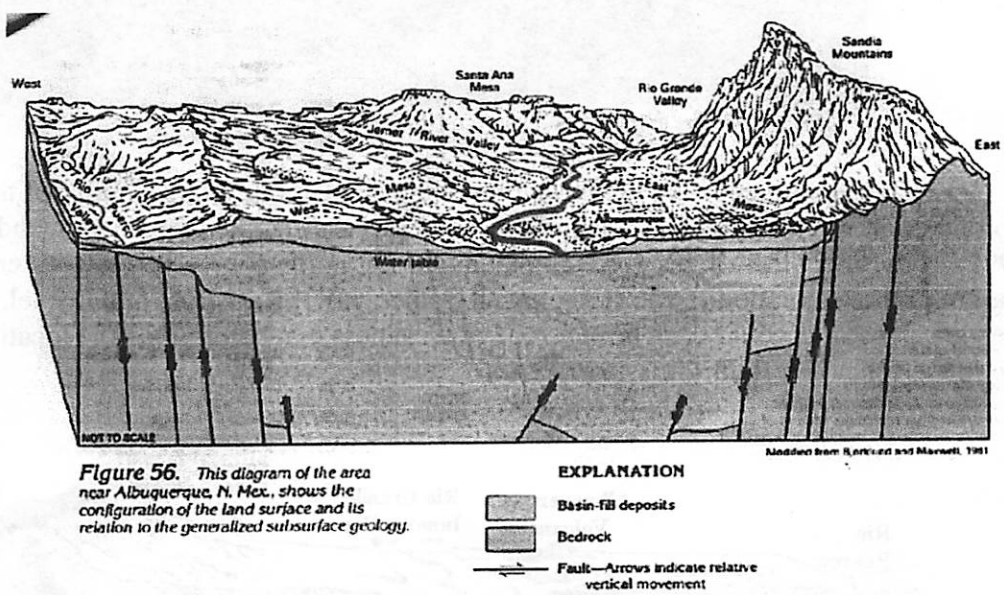

Figure 56. This diagram of the area near Albuquerque, N. Mex., shows the configuration of the land surface and its relation to the generalized subsurface geology.

Figure showing sediment and volcanically filled rift basin.
(Image courtesy of (Bjorklund and Maxwell, 1981), from
http://academic.emporia.edu/schulmem/hydro/TERM%20PROJECTS/Kuss/Hydrogeo%20Term%20Project.html)

The "…individual basins of the rift are typically asymmetrical". "The main basins…" "…are commonly themselves divided by intrabasin horsts". "Grabens are terminated along structurally complex zones (transfer faults and accommodation zones) which transfer fault offsets to adjacent grabens…". The "…adjacent grabens are typically tilted in the opposite directions and separated by northeast-striking transfer zones…" (Keller and Baldridge, 1999).

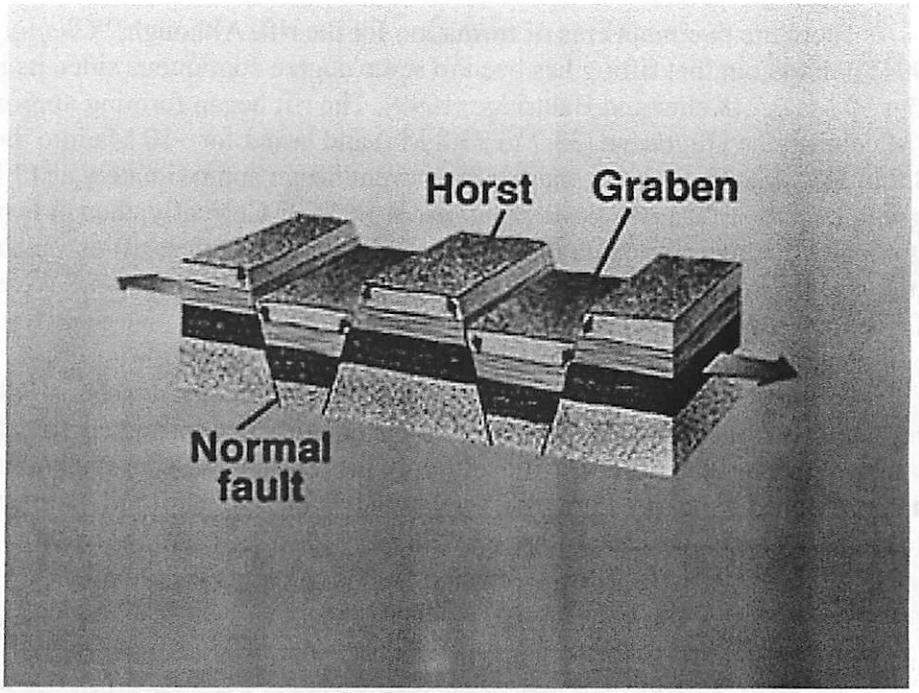

Horst and Graben Diagram (Image Courtesy USGS)

"One way to envision the formation of the Rio Grande rift is simply for the Colorado Plateau to rotate 1-1.5 degrees in a clockwise direction (e.g. Chapin and Cather, 1994). If north-south striking strike-slip faults for Laramide age formed the eastern margin of the Colorado Plateau (Chapin and Cather, 1981; Karlstrom and Daniel, 1993), then these features could have been a zone of weakness that determined the location of the rift" (Keller and Baldridge, 1999).

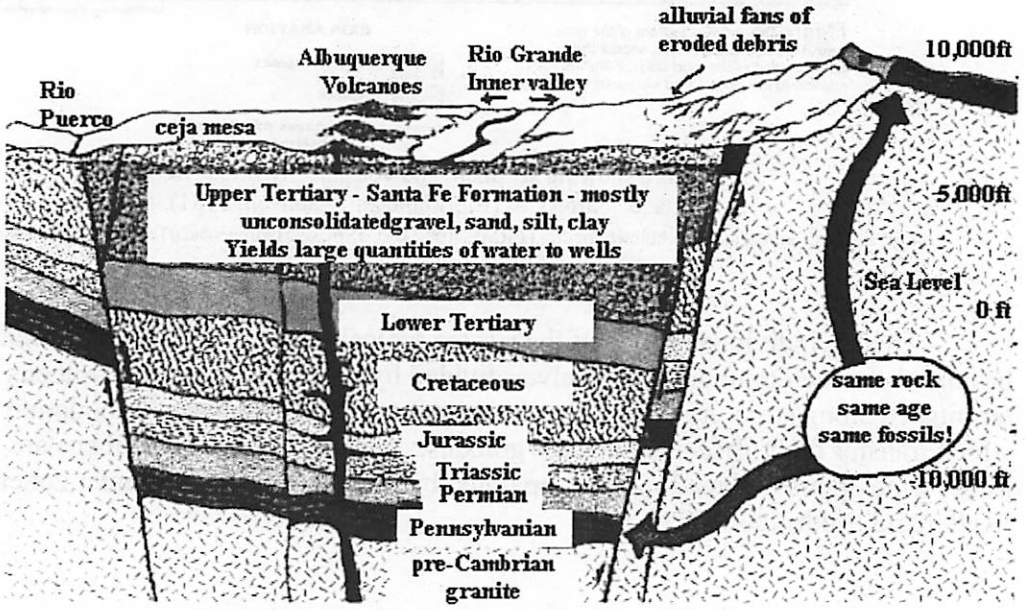

Image from (http://www.cabq.gov/aes/s1geol.html)

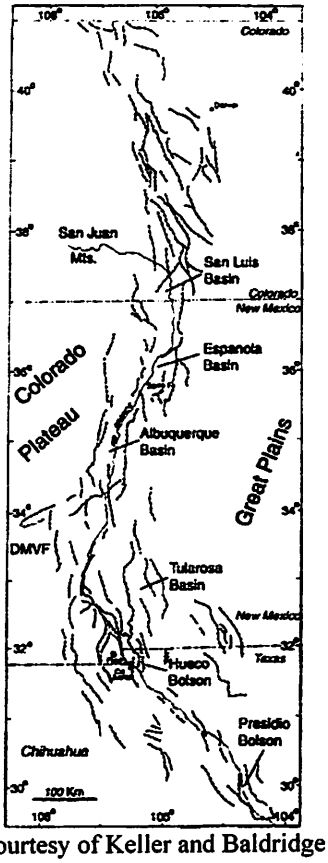

(Image Courtesy of Keller and Baldridge (1999))

References

Chapin, C. E., and Cather, S. M., 1981. Eocene tectonics and sedimentation in the Colorado Plateau-Rocky Mountain area. *Arizona Geological Digest*, v. 14, p. 173-198.

Chapin, C. E., and Cather, S. M., 1994. Tectonic setting of the axial basins of the northern and central Rio Grande rift, in Keller, G. R., and Cather, S. M. eds., Rio Grande rift: Structure, stratigraphy, and tectonic setting: *Geological Society of America Special Paper* 291, p. 5-25.

Karlstrom, K. E., and Daniel, C. G., 1993. Restoration of the Laramide right-lateral strike-slip in northern New Mexico by using Proterozoic piercing points. *Geology*, v. 21, p. 188-211.

Keller, G. R. and Baldridge, W. S., 1999. The Rio Grande rift: A geological and geophysical overview. *Rocky Mountain Geology*, v. 34, no. 1, p. 121-130.

http://home.att.net/~sgeoveatch/rio_grande_rift.htm

http://en.wikipedia.org/wiki/Rio_Grande_Rift

White Sands Missile Range and Space Exploration

Nikole Lewis

Introduction

Although the history of rocketry in New Mexico first began in the 1930s with the arrival of Dr. Robert H. Goddard in Roswell, NM, it was the work done at the White Sands Missile Range (WSMR) that helped to propel our country into the space age. The White Sands Proving Ground was established on July 9th, 1945 as the primary site for U.S. rocket testing and development. At the close of World War II, White Sands became home to handful of German scientists and a vast inventory of V-2 rocket parts. These V-2 rockets were the seeds from which the American space program grew. Today, WSMR still supports both the manned and scientific exploration of space.

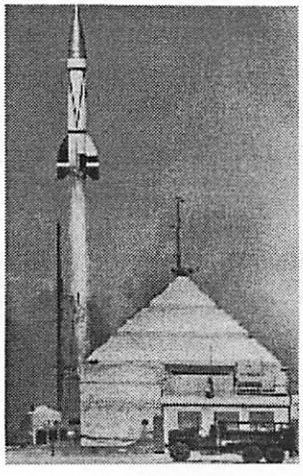

Figure 1: Historic Launch Complex 33

WSMR and Early Rocketry

Perhaps the most famous rocket to be launched from the the WSMR is the V-2. The V-2 rocket was developed in Germany by Dr. Wherner von Braun and then moved to WSMR at the end of World War II. In all 67 V-2 rockets were tested and assembled at WSMR between 1946 and 1952. These launches were not only weapons tests. Several scientific experiments were put aboard the V-2's to study the Earth's upper atmosphere and determine the biological impact of high altitude flight. Additionally, the *Bumper* project was the first to study staged rockets using V-2 components.

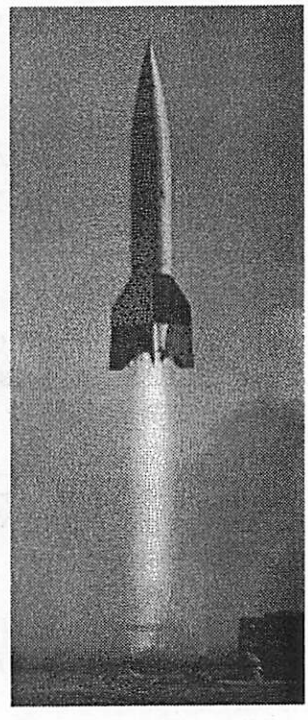

Figure 2: Launch of V2 Rocket from WSMR.

From the V-2 sprung the Redstone rocket, developed by von Braun at Redstone Arsenal. It was the Redstone rocket that propelled the

first U.S. satellite and man into space. The Aerobee class of rockets was also developed at WSMR. Between 1948 and 1958, around 165 Aerobee rockets had been successfully launched carrying payloads to study the upper atmosphere and cosmic radiation.

Figure 3: Image of White Sands taken from a V-2 rocket.

NASA and the WSMR

The White Sands Test Facility (WSTF) was established in 1963 on the grounds of the WSMR as part of the NASA Johnson Space Center. The WSTF has been heavily involved in propulsion and materials development and test for the manned space program. Additionally, the WSTF has served as the proving ground for such technologies as the Pepp Aeroshell used for the Viking Mars Landing.

The WSTF also operates the White Sands Space Harbor (WSSH), which includes two laser-leveled lakebed runways that serve as an alternate shuttle landing site. All shuttle pilots train at the WSSH using modified Gulfstreams to simulate shuttle landings. NASA also launches most of its sounding rocket missions from the WSMR. The sounding rocket experiments are generally launched atop a Black-Brant rocket and are used as a low cost way for scientists to obtain data above Earth's lower atmosphere or in a microgravity environment.

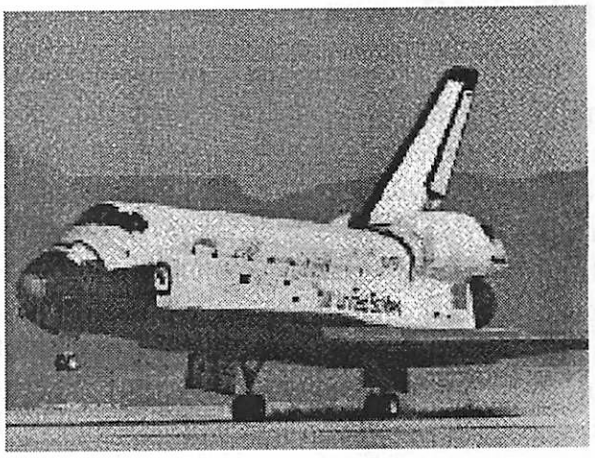

Figure 4: Shuttle Columbia landing at WSMR.

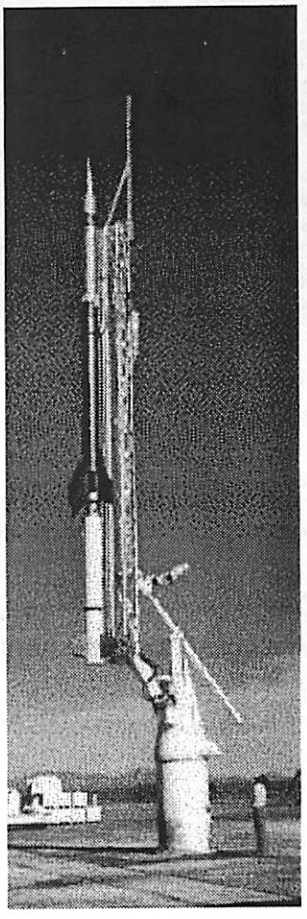

Figure 5: The Black-Brant Sounding Rocket.

The Future of Space Exploration at WSMR

NASA still plans to make extensive use of the WSMR for the Orion spacecraft for testing the launch abort system and as a possible landing site. Perhaps a more exciting prospect for the future of space exploration at White Sands is the development of Spaceport America. While not on WSMR proper, it is in close proximity to take advantage of the restricted airspace in the region. Spaceport America will provide the facilities and resources necessary for private sector space exploration to grow.

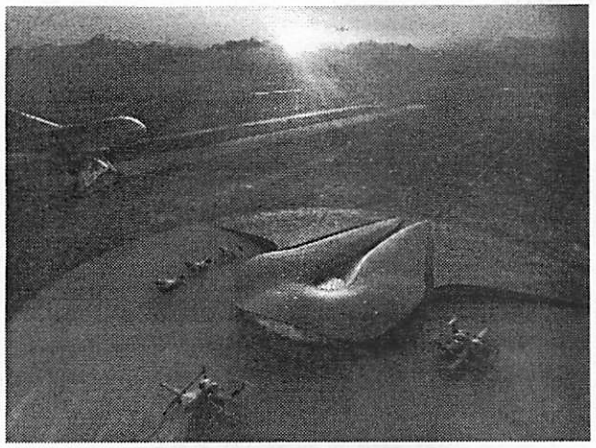

Figure 6: Artist vision of Spaceport America in White Sands, NM.

References

World Spaceflight News 2003, 21st Century Complete Guide to White Sands. Mt. Laurel, NJ: Progressive Management.
http://www.spaceportamerica.com/
http://rscience.gsfc.nasa.gov/
http://en.wikipedia.org/wiki/Aerobee

Gypsum Sources at White Sands

What makes the sands of White Sands National Monument so white is their composition? Instead of the usual quartz variety, this sand formed from gypsum.

Where did the gypsum come from?
If you look around to the mountains surrounding the dune field you'll see the Sacramento Mountains to the east and the San Andres Mountains to the west. These are the sources of the gypsum. But to understand why these mountains have gypsum in them it is necessary to understand the circumstances of their formation.

Yeso Formation (~250 Ma)

(Permian Period at the end of the Paleozoic Era- 570-245 Ma)

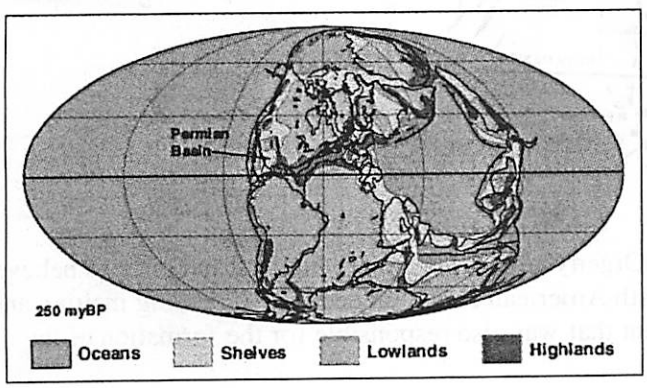

During the Paleozoic Era most of New Mexico was covered by shallow seas. In the beginning of the Permian Period North America was part of the mega continent Pangaea and New Mexico was still submerged in a tropical sea, just south of the equator, the Permian Basin. But in the middle of the Permian Period there was a major fall in sea level, which caused large portions of New Mexico to dry up. This led to the deposition of 1500 feet of gypsum in what is referred to as the Yeso Formation.

{*Gypsum Formation*: Gypsum is an evaporite, meaning it forms when dissolved ions become concentrated due to water evaporation. If sea water is reduced to 20% of its original volume through evaporation then calcium (Ca2+) and sulfate ($SO_4$2-) ions it will be concentrated enough for gypsum to form.}

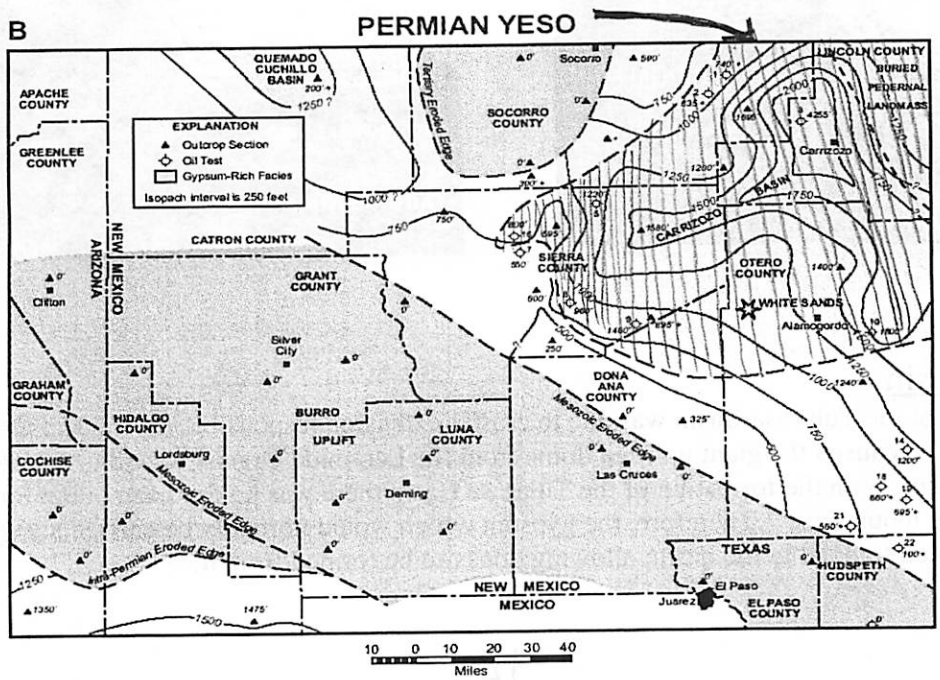

Laramide Uplift

(End of the Cretaceous Period ~70 Ma)

During the next few hundred years this gypsum was buried under sediments until the Laramide Orogeny uplifted the Permian marine rocks into a dome shape in the White Sands region.

MAJOR LARAMIDE STRUCTURAL FEATURES OF SOUTH-CENTRAL NEW MEXICO

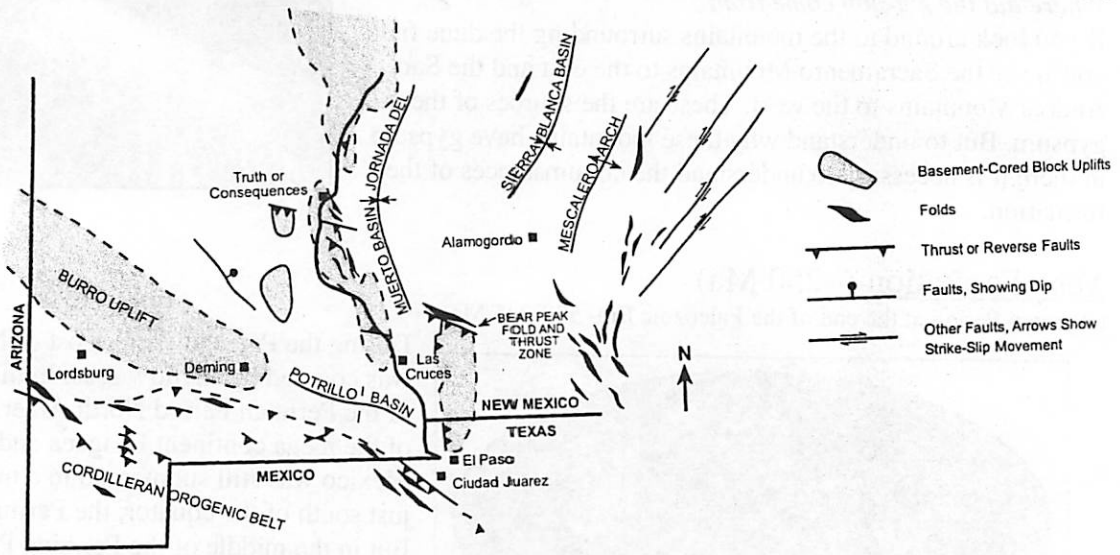

{Laramide Orgeny: The causes of the Laramide Orgeny are not completely understood but it is believed the angle of the plate subducting beneath the North American continent decreased, moving melting and mountain building much further inland. This event that was also responsible for the formation of the Rocky Mountains.}

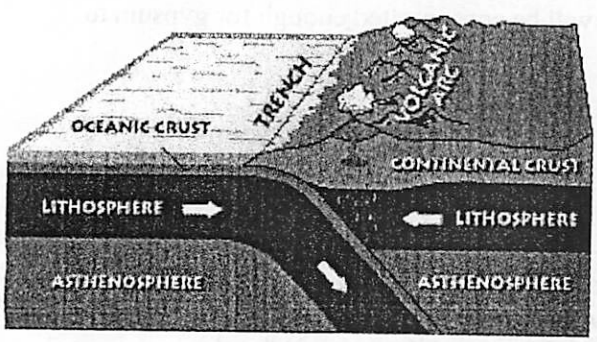

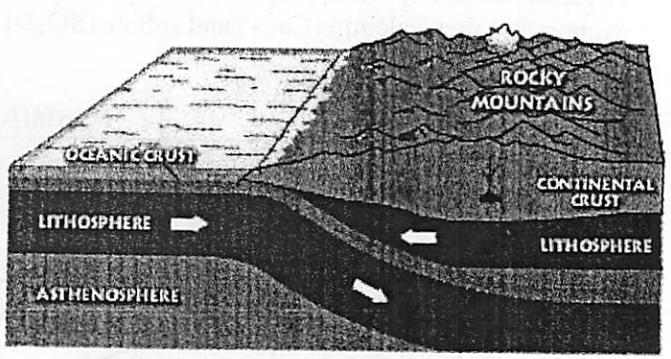

Tularosa Basin

The formation of the Tularosa Basin was due to crustal extension responsible for the Rio Grande Rift (Devin's Talk). It caused the giant uplifted dome from the Laramide Orgeny to collapse at its center forming the basin. With the formation of the Tularosa Basin there was no drainage outlet for runoff from the surrounding mountains. Therefore, the gypsum which would normally be carried away by rivers or streams, is instead trapped in the basin, allowing dunes to be formed from it.

Scaling of Megaripples and Transverse Dunes
by: Serina Diniega

1 Physical background

Dunes and ripples are landforms created and evolved due to interactions between a fluid (in this case: air) and granular material (sand grains). Saltation and reptation (see figure 1) are the primary grain motions involved; creep does play a small role in the formation, but will be neglected in this study.

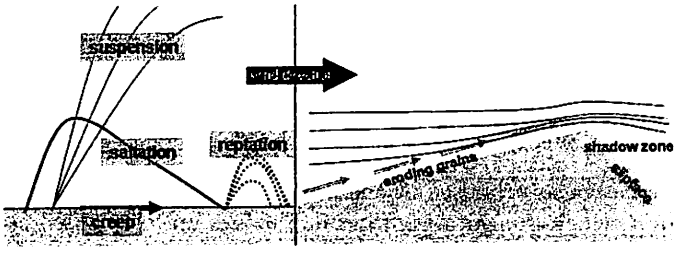

Figure 1: On the left: illustrations of the processes which occur through air-sand, sand-sand interactions. On the right: profile of a dune. The asymmetry is due to the different processes moving grains: on the upwind side, grains bounce up the slope and over the crest of the dune, pushed by the wind. Once they pass the crest, they fall into the "shadow zone" where there's no strong air current and freefall down onto the slipface, where avalanching is the dominant grain motion process. In total, the sand is moved from left → right and the dune moves forward.

The wind's shear stress velocity u_* is the measure of how hard the wind is blowing. It appears in the Prandlt-von Karman relation: $u(z) = \frac{u_*}{\kappa} \ln \frac{z}{z_o}$, which gives the wind velocity at height z as a function of the surface roughness (z_0) and the shear stress velocity (u_*) (κ is a constant).

A minimum amount of shear stress is needed to initiate grain motion: $u_{*,th} \sim \sqrt{\frac{\rho_{sand} - \rho_{air}}{\rho_{air}} gd}$. Once $u_* > u_{*,th}$, then sand grains are entrained into the airflow (momentum is transferred from the air to the grains).

The maximum amount of sand grains which can be carried is limited by how hard the wind is blowing, as at some amount of moving grains the amount of momentum "carried" by the air is not sufficient to continue initiating sand motion (this is called the Owen's criterion). Empirically, this has been found to be $\sim u_*^3$ (starting with Bagnold (1941) and refined many times since then).

2 Grain motion length scale

The characteristic length of saltating grains is found by approximating their trajectories as ballistic: saltation length $l_{salt} \sim u\frac{w}{g}$, where u is the average horizontal velocity of the grains, and w is the initial vertical velocity of the saltating grain. If we assume $u,\ w \sim u_*$, then $l_{salt} = a\frac{u_*^2}{g}$, where a is the proportionality constant.

As the motion of reptating grains is induced by impacts from saltating grains, then we can assume that the number of reptating grains (N_{rep}) is proportional to the number of saltating grains (N_{salt}). That proportionality constant will depend on the energy is exchanged in the impact, so will be based on material properties, the impact velocity of the saltating grain (assumed $\sim u_*$), and the ejection velocity of the reptating grains (assumed $= \sqrt{dg}$, where d is the grain diameter). So, the "efficiency of the erosion process" $= \gamma = \frac{N_{rep}}{N_{salt}} = k\frac{u_*}{\sqrt{dg}}$, where k averages together material effects and energy-transfer efficiency, but is independent of g and u_*.

If we assume reptating grains also travel on ballistic trajectories (a more valid assumption than for saltating grains) with the ejection velocity given above, then the distance traveled by the reptating grains is $l_{rep} = bd$ (where b is a proportionality constant), and independent of u_*.

Thus, if we'd like to know the "average" trajectory length, we can use $L = \frac{N_{rep}l_{rep}+N_{salt}l_{salt}}{N_{rep}+N_{salt}} = u_*\frac{bkd+au_*\sqrt{d/g}}{ku_*+\sqrt{gd}}$. In the limit of u_* large, note that $L/l_{salt} \to \frac{\sqrt{dg}}{ku_*} = \frac{N_{salt}}{N_{rep}} = \gamma^{-1}$.

3 Other length scales

The length scale that has been proposed as the important scale for dunes is the saturation length scale: the distance over which the saltating sand flux moves up to its maximal amount.

Approximating the moving sand layer as two distinct layers of saltating grains and reptating grains (i.e., reptating grains do not accelerate to become saltating grains), then the saturation distance should be related to L. In fact, it was derived to be: $l_{sat} = L\frac{u_{*,th}^2}{u_*^2-u_{*,th}^2} = \frac{l_{salt}}{\gamma}\frac{u_{*,th}^2}{u_*^2-u_{*,th}^2}$. The additional term represents how quickly the energy will be transferred from the air to the saltating grains (Sauermann et al. 2001 Kroy et al. 2002);

However, if we assume that reptating grains are accelerated up to become saltating grains, then this changes how the energy is exchanged between the air and the grains. In this case, the distance over which reptating grains are accelerated up to become saltating grains is the relevant length scale: $l_{drag} \sim \frac{\rho_{sand}}{\rho_{air}}d$ (Andreotti et al. 2002). Note that $l_{drag} \sim l_{salt}|_{u_{*,th}}$; the proportionality factor probably relates to the number of bounces needed.

4 Parameters on different planets

Here are relevant environmental parameters and calculated variables (the Earth values were used to find the coefficients, they were taken from Andreotti et al. (2002) and are empirical).

	d (μm)	g (m/s^2)	ρ_{fluid} (kg/m^3)	ρ_{grain}	$u_{*,th}$ (m/s)	$\gamma|_{u_{*,th}}$	l_{salt} (m)	l_{rep}	L	l_{drag}
Earth	200	9.8	1.225	2650	0.2	0.2	0.5	0.008	2.5	9
Mars	500	3.7	0.016	3200	2	2	116	0.02	60	2100
	87[1]	3.7	0.016	3200	0.8	2	20	0.004	10	360
	500	3.7	0.016	3200	5[2]	5	822	0.02	160	2100
flood?	1e6	3.7	1000	3200	0.3	0.006	2.5	4	400	67
Venus	100[1]	8.9	61	3200	0.02	0.03	0.006	0.004	0.2	0.1
Titan	200?	1.4	5	1000	0.02	0.06	0.05	0.008	0.8	0.8

Here are the relative scales (to an order of magnitude), with those matching up with observations highlighted. Unfortunately I did not find particle sizes of terrestrial subaqueous dunes forming under catastrophic flood conditions, so were unable to directly compare those scales (maybe someone has an estimate?).

	E:M:V:T
actual scaling of dune spacing	20:600:?:? ~ 1:10:?:?
l_{salt}	0.5:116:0.006:0.05 ~ 1:100:0.01:0.1
	0.5:20:0.006:0.05 ~ **1:10**:0.01:0.1
	0.5:822:0.006:0.05 ~ 1:1000:0.01:0.1
L	2.5:60:0.2:0.8 ~ **1:10**:0.1:1
	2.5:10:0.2:0.8 ~ 1:1:0.1:1
	2.5:160:0.2:0.8 ~ 1:100:0.1:1
l_{drag}	9:2100:0.1:0.8 ~ 1:100:0.01:0.1
	9:360:0.1:0.8 ~ **1:10**:0.01:0.1

5 Megaripples

The different size scale of ripples (compared to dunes) is thought to be due to the relative importance of reptation to saltation: in dunes, it is thought that most motion and the length scale are dominated by saltation, and reptation primarily adds some lateral diffusion to the system. However, reptation scales (which are hypothesized to be primarily set by d) are closer to observed spacing of ripples.

In comparing megaripples on the Earth (large, asymmetric ripples composed of bimodally sized coarse/fine material, with spacings of $> 50cm$) and Mars, we see very similar sizes (cm-10m in height, 1m-100m in spacing), with the extreme-large end of the scale occuring during catastrophic floods (where much larger particles are moved). The main difference is in the height-to-spacing ratio (the ripple index), which is half as large on Mars.

	E:M
actual scaling of megaripple height	0.05-0.6[3]-13[4]:0.15[5]-5.7[6] ~ 1-10-100:1-100
actual spacing of megaripple spacing	0.7-10[3]-100[4]:1.5[5]-38[6]-70 (see figure 2) $\sim 1-10-100:1-10-100$
ripple index (spacing:height)	15:7

References

Andreotti, B., Claudin, P. Douady, S. (2002), 'Selection of dune shapes and velocities, Part 1: Dynamics of sand, wind, and barchans', *The European Physical Journal B* **28**, 321–339.

Bagnold, R. A. (1941), *The physics of blown sand and desert dunes*, Methuen.

Claudin, P. Andreotti, B. (2006), 'A scaling law for aeolian dunes on Mars, Venus, Earth, and for subaqueous ripples', *Lunar and Planetary Science Letters* .

Greeley, R., Bridges, N. T., Kuzmin, R. O. Laity, J. E. (2002), 'Terrestrial analogs to wind features at the Viking and Pathfinder landing sites', *Journal of Geophysical Research* **107**, E1, 5005.

Kroy, K., Sauermann, G. Herrmann, H. J. (2002), 'Minimal model for aeolian sand dunes', *Physical Review E* **66**(3), 031302–1 – 18.

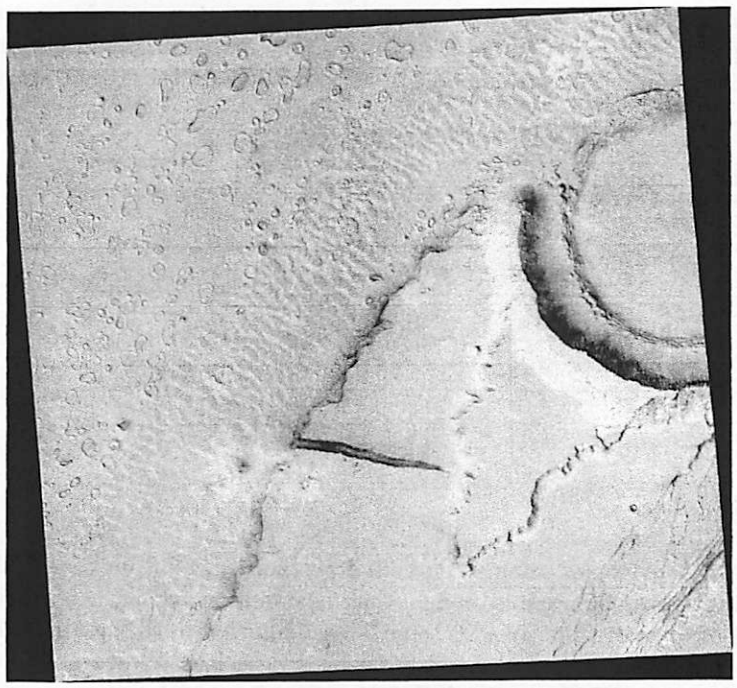

Figure 2: MOC2-862a: cPROTO image R12-03203, Athabasca Vallis Flood Megaripples. This high-resolution (1.5-.5m/pixel) image (3km wide) was taken to look for boulders in these exhumed megaripples formed by an ancient catastrophic flood in Mars' Athabasca Vallis – the size of the ripples implies that the "mean" particle size should be on the order of 0.1-1m, and finding boulders in the ripples would help constrain estimates of the power of the floods. However, the image does not show boulders in the ripples, implying either that the rocks that make up these features have diameters less than in diameter or that the ripple sediments have not been completely exhumed. North is up and sunlight illuminates the scene from the lower left. Photo Credit: NASA/JPL/Malin Space Science Systems.

2. Pollack, J. B., Haberle, R. Greeley, R. (2006), 'Estimates of the Wind Speeds Required for Particle Motion on Mars', *Icarus* **29**, 395 – 417.

Sauermann, G., Kroy, K. Herrmann, H. J. (2001), 'Continuum saltation model for sand dunes', *Physics Review E* **64**(3), 031305–1–10.

3. Williams, S. H., Zimbelman, J. R. Ward, A. W. (2002), Large Ripples on Earth and Mars, *in* 'Lunar and Planetary Institute Conference Abstracts', pp. 1508–+.

6. Yizhaq, H. (2005), 'A mathematical model for aeolian megaripples on Mars', *Physica A* **357**, 57 – 63.

4. catastrophic flood in Washington State (Scabland)

Radarclinometry of Dune Fields

by Catherine Neish

Introduction to Radarclinometry

SAR (synthetic aperture radar) images are formed when radio waves are directed towards a planetary surface, and the waves are scattered back to the dual transmitter/receiver (Figure 1).

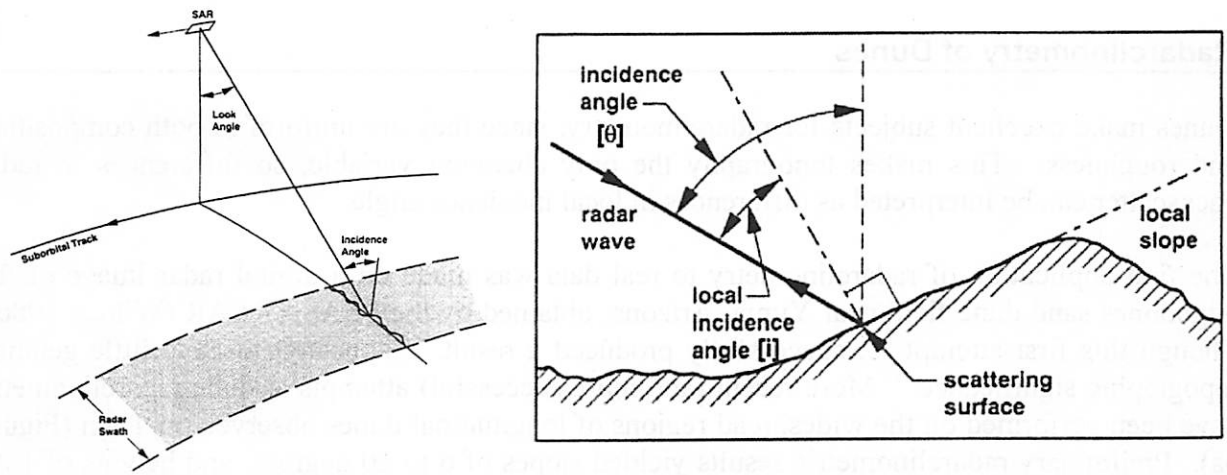

Figure 1: Geometry of radar image acquisition. The incidence angle, θ, is roughly the same as the SAR look angle, though it may be affected by planetary curvature. The local incidence angle, i, is affected by local topography.

Radar images of planetary surfaces provide a wealth of information about the surface being imaged, because radar backscatter depends on three main surface properties (Figure 2):

- Topography
  - → Effects the local incidence angle
- Roughness
  - → Effects the direction of the backscatter
- Composition
  - → Effects the dielectric constant

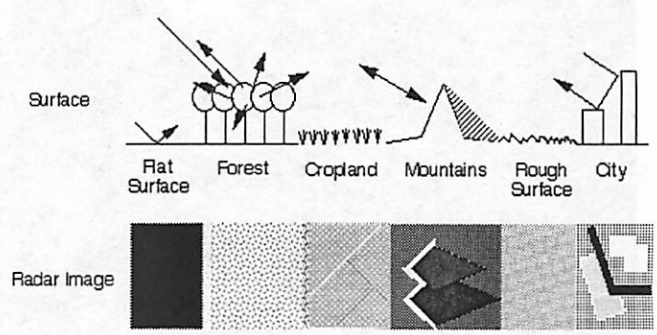

Due to the dependence of radar backscatter on incidence angle, an individual SAR image can reveal topography by radarclinometry, or "shape-from-shading" (Wildey 1986). Given a radar backscatter value, σ^0, the local incidence angle, i, is determined by inverting a relevant scattering model, $\sigma^0 = f(i)$. Scattering models are generally based on global scatterometry data, and vary depending on the roughness of the surface being studied (Figure 3).

Once the observed backscatter profile is converted to local incidence angles using an appropriate scattering model, a topographic profile is reconstructed from the set of calculated angles. This technique is limited in the sense that σ^0 does not depend exclusively on topography, but also on roughness and composition, which are neither known in an absolute sense, nor are they certain to remain constant across a given feature.

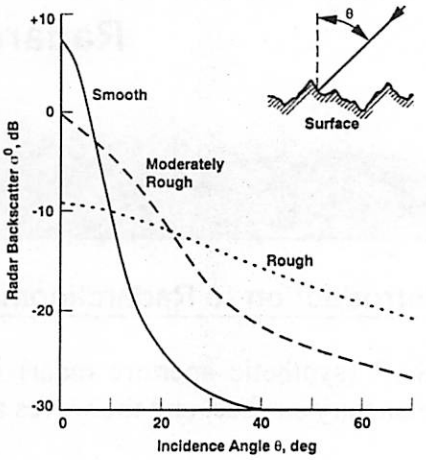

Figure 3: Radar backscatter as a function of incidence angle for representative surfaces.

Radarclinometry of Dunes

Dunes make excellent subjects for radarclinometry, since they are uniform in both composition and roughness. This makes topography the only changing variable, so differences in radar backscatter can be interpreted as differences in local incidence angle.

The first application of radarclinometry to real data was made on a digital radar image of the Algodones sand dune field near Yuma, Arizona, obtained by the SEASAT SAR (Wildey 1986). Though this first attempt "...successfully produced a result, it appeared to have little genuine topographic significance." More recent (and more successful) attempts at dune radarclinometry have been performed on the widespread regions of longitudinal dunes observed on Titan (Figure 4a). Preliminary radarclinometric results yielded slopes of 6 to 10 degrees, and heights of 100-150 m (Lorenz et al. 2006). The spacing and height are typical of dunes observed in the Namib desert (Figure 4b).

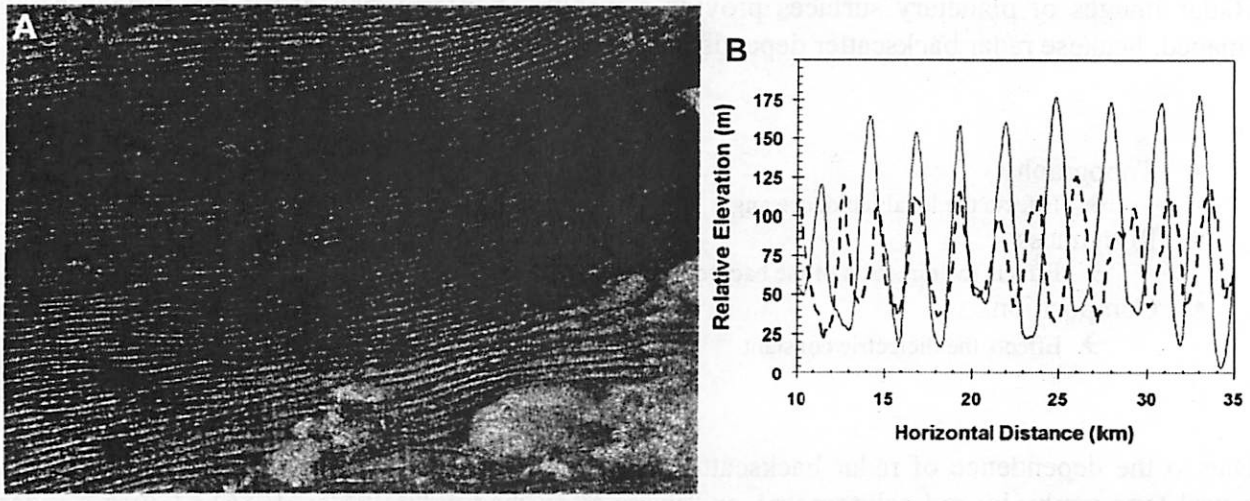

Figure 4: (a) A Cassini RADAR image of a sand sea on Titan (235 km by 175 km at 12 S, 100 W). The radar illumination is from the top. (b) Radarclinometric profile of the dunes shown in (a) (solid line). The spacing and height are typical of Namib desert dunes, shown by the dashed line (from Shuttle Radar Topography Mission data).

Validation of the Technique

(aka Radarclinometry vs. Reality)

Given the many assumptions and approximations inherent in radarclinometry, it's instructive to validate the technique using independent sources of topography. This gives us an understanding of how robust the technique is when applying it to planets where no independent source of topography is available.

No SAR is available over the White Sands area, so I instead analyzed a Spaceborne Imaging Radar (SIR-C) image taken over the dunes in the vast Namib Desert (Figure 5). I then compared the resultant height profile to topography data obtained by the Shuttle Radar Topography Mission (SRTM), to determine the reliability of radarclinometry in determining the topography of sand dunes (Figure 6).

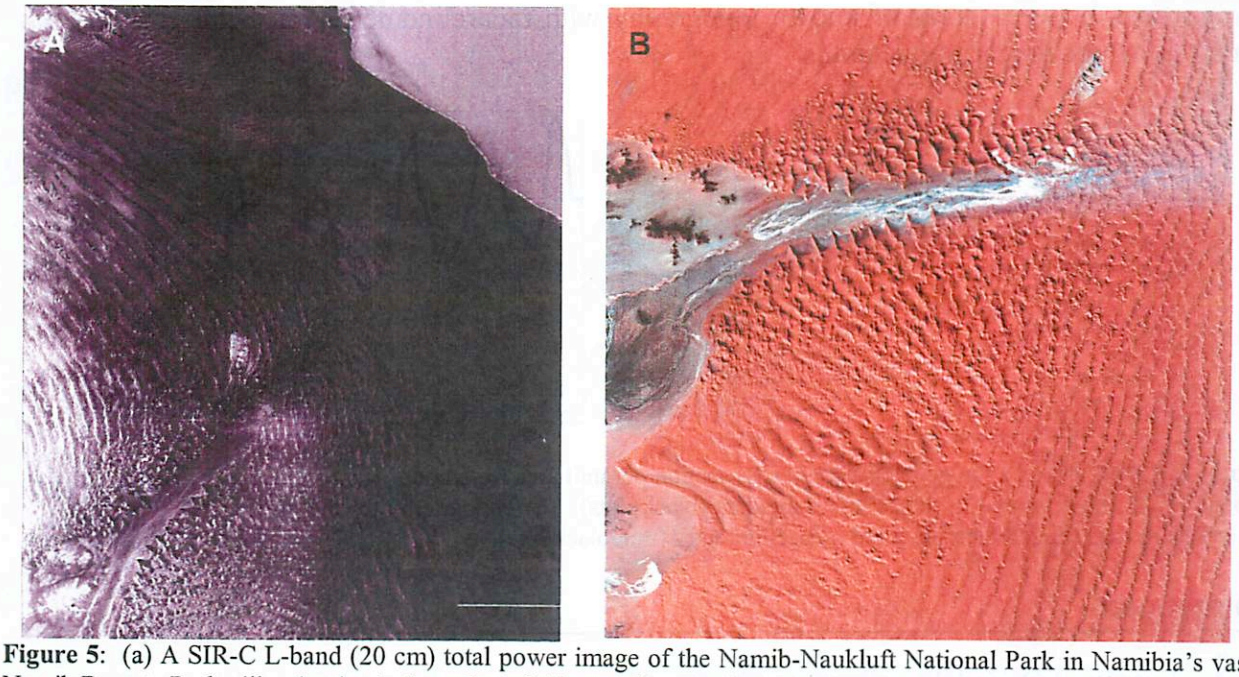

Figure 5: (a) A SIR-C L-band (20 cm) total power image of the Namib-Naukluft National Park in Namibia's vast Namib Desert. Radar illumination is from the left (the southeast). (b) A Landsat image of the same region.

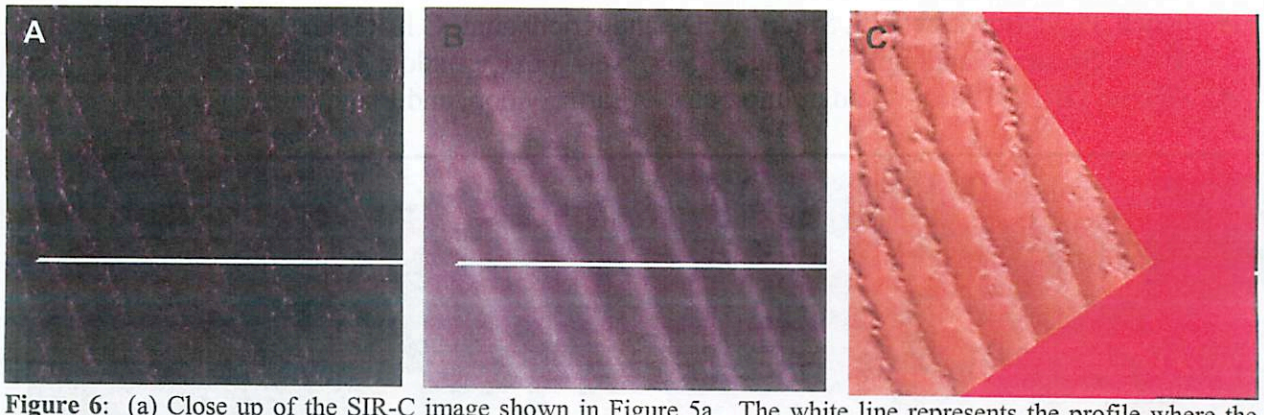

Figure 6: (a) Close up of the SIR-C image shown in Figure 5a. The white line represents the profile where the radarclinometry will be performed. (b) SRTM topography data from the same region. The white line represents the profile where the topography profile will be extracted. (c) A Landsat image from the same region.

To conduct the radarclinometric analysis, I first had to find an appropriate scattering model for the dunes. I used the model given for smooth, gently sloping, dry desert sand given by Ruck et al. (1970), scaled to the observed change in backscatter over the SIR-C radar image (Figure 7a). The results of the analysis, compared to the actual topography of the region, are shown in Figure 7b. There is good agreement between the radarclinometric profile and the topography for the first two dunes. At the third dune, it appears that the sand takes on different scattering properties, causing a disagreement between the radarclinometric profile and the measured topography. This could be due to the sand layer thinning and revealing the interdune material underneath. The interdune material is presumably of a different composition than the sand, and therefore would have different scattering properties (recall the dependence of backscatter on dielectric constant).

Given this initial comparison, it's clear that one must be careful when using radarclinometry to determine the topography of a planetary surface for which topography is unknown. However, comparisons between areas of known topography with radarclinometry can help us determine when and where the technique holds.

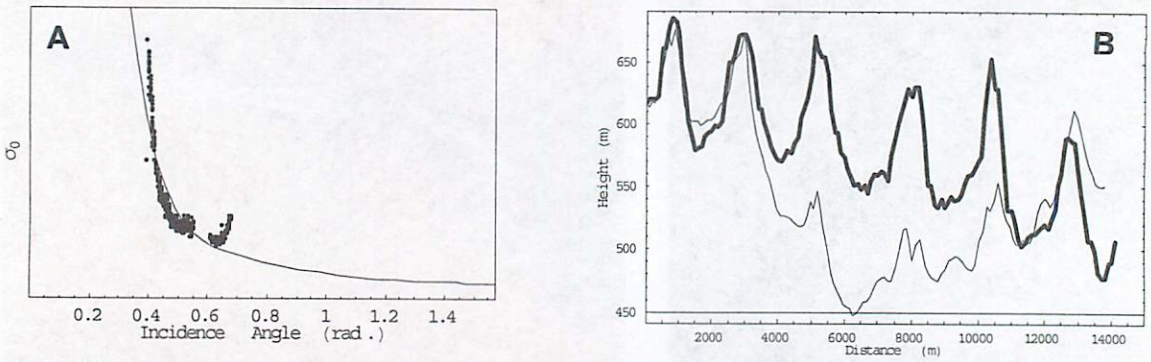

Figure 7: (a) Measured average backscatter cross section per unit area for smooth, gently sloping, dry desert sand at X-band (3 cm; line), scaled to the Namib dune data (black dots). (b) Topography for the profile shown in Figure 6 using SRTM data (thick black line) and radarclinometry (thin black line).

References

- Lorenz, R.D. and 39 colleagues (2006). "The sand seas of Titan: Cassini RADAR observations of longitudinal dunes." Science 312, 724-727.
- Ruck, G.T., Barrick, D.E., Stuart, W.D., and Krichbaum, C.K. (1970). "The Radar Cross-Section Handbook." Plenum Press, New York, London, 453 pp.
- Wildey, R.L. (1986). "Radarclinometry." Earth, Moon, and Planets 36, 217-247.

The Trinity Nuclear Test

by David Choi

Abstract: The "Trinity" Nuclear Test, conducted by the United States of America as the culmination of the Manhattan Project, was the first explosion of a nuclear weapon. It occurred on the early morning of 16 July 1945 near Socorro, New Mexico, on what is now the White Sands Missile Testing Range. The explosion's power was the equivalent of 20 kilotons of TNT and was a test of an implosion-design plutonium bomb, later used above Nagasaki before the surrender of Japan and the end of World War II.

Figures

(right) An aerial shot of the base camp established near the Trinity test site.

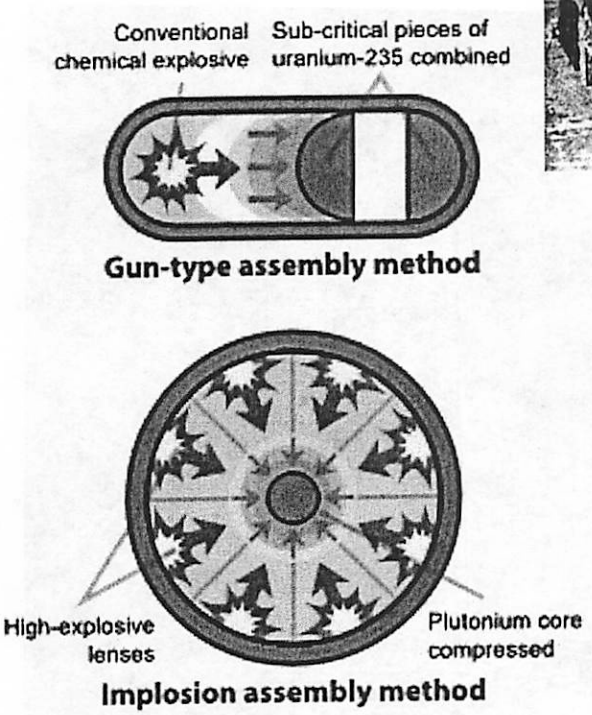

(above left) The two types of nuclear bombs designed in the Manhattan Project. The gun-type assembly uses conventional explosives to combine uranium-235 to create a critical mass and produce a nuclear explosion. The implosion-type uses conventional explosives and an explosion lens to direct the energy into compressing a plutonium core, creating a critical mass and a nuclear explosion.

(right and below) "The Gadget" is hoisted to the top of the test tower.

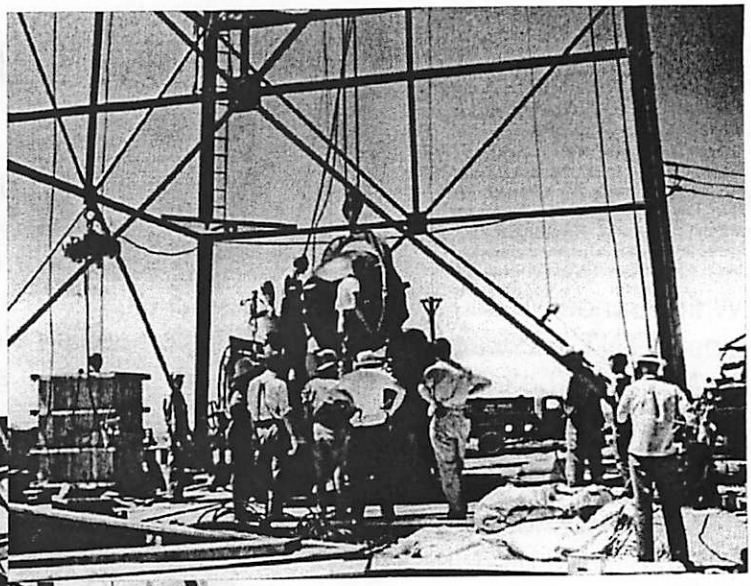

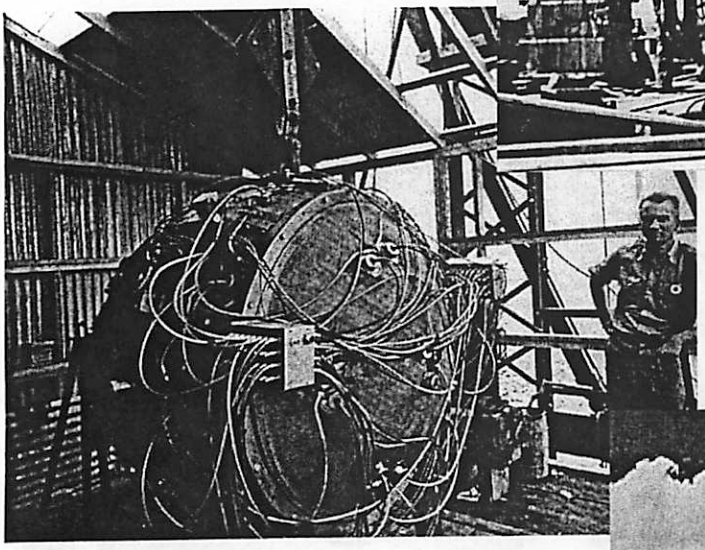

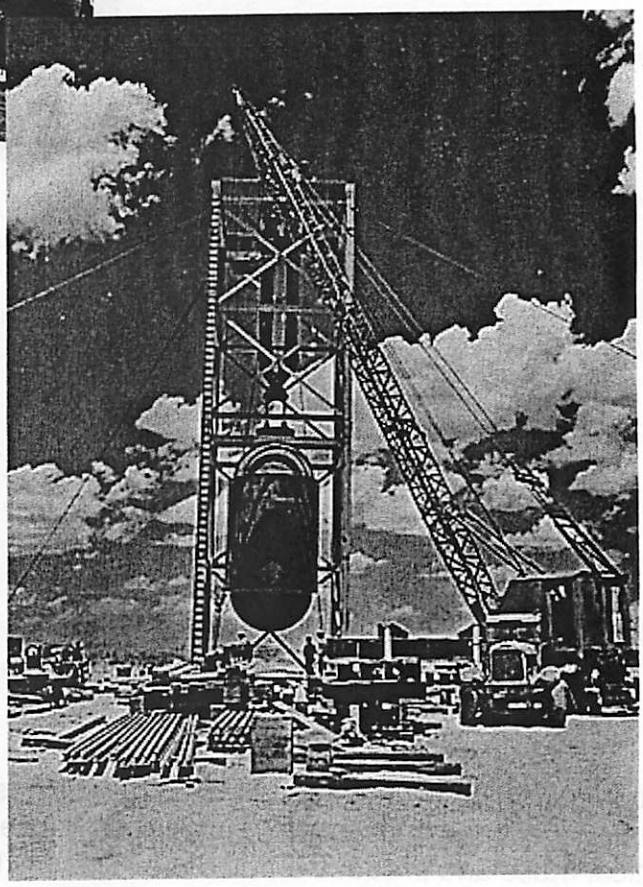

(right) "Jumbo", the large steel canister designed to host the device in case of an explosion that did not trigger a nuclear chain reaction. Although great efforts were made to transport the structure to the test site, ultimately it was not used as the scientists were confident that the bomb's design would successfully trigger a chain reaction. It was placed 800 yards away under a steel tower to gauge the energy of the explosion. "Jumbo" survived, the tower did not.

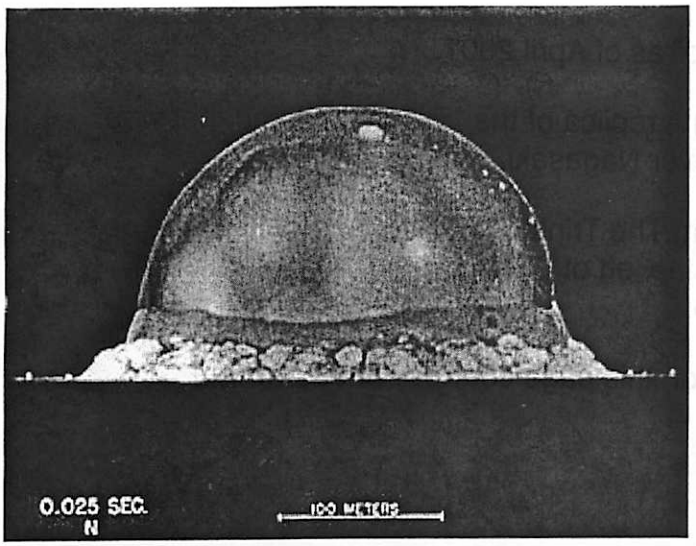

(left) A photograph of the fireball from the Trinity test, taken 0.025 seconds after the explosion.

(below left) The mushroom cloud formed by the Trinity blast.

(below right) An aerial view of ground zero, the day after the explosion.

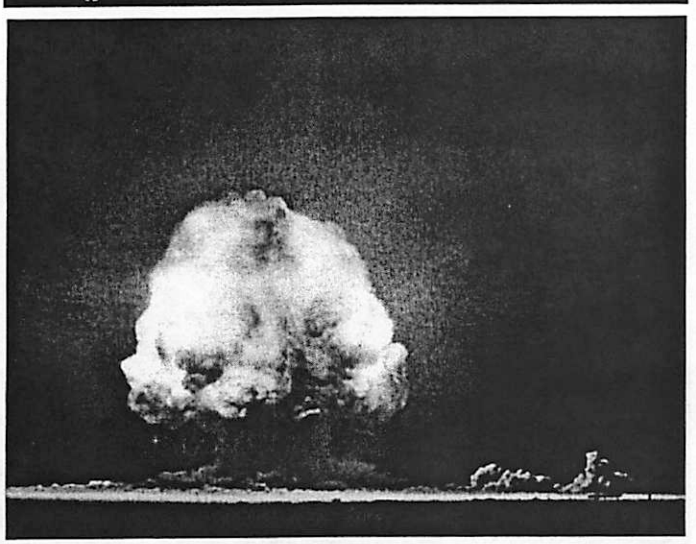

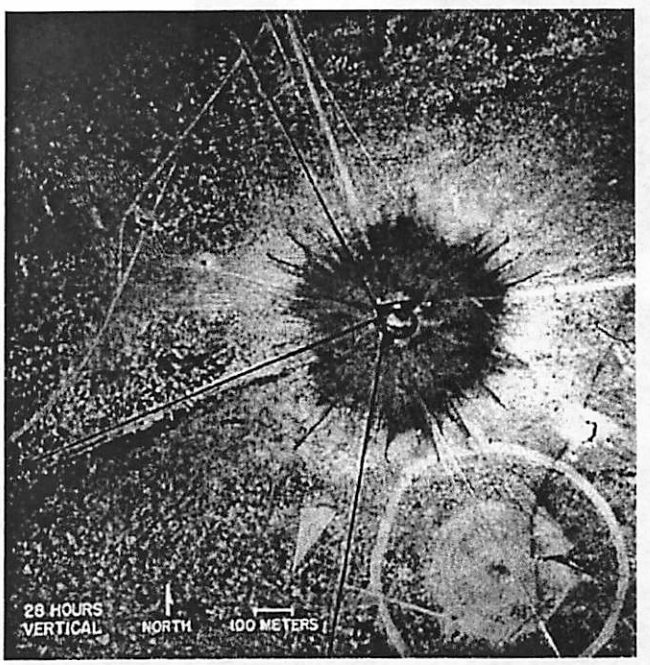

(below left) A map of the levels of nuclear fallout after the blast.

(below right) Army officials, scientists, and media examine the remains of the tower at ground zero after the test.

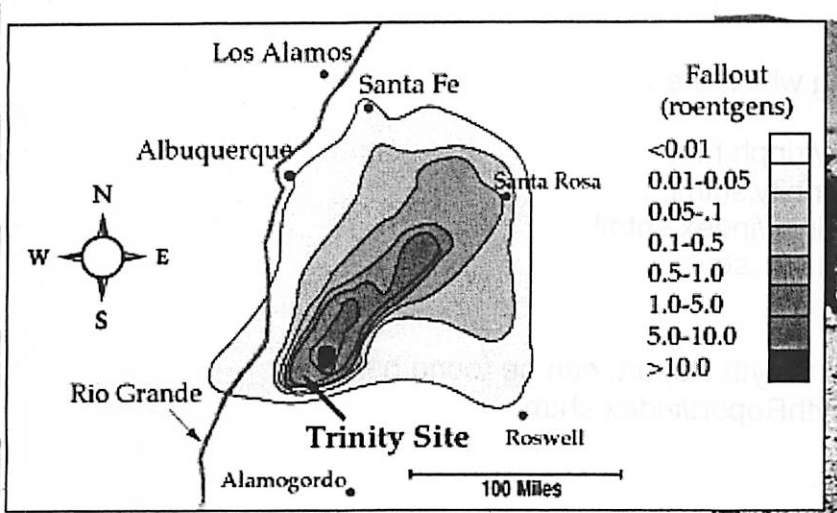

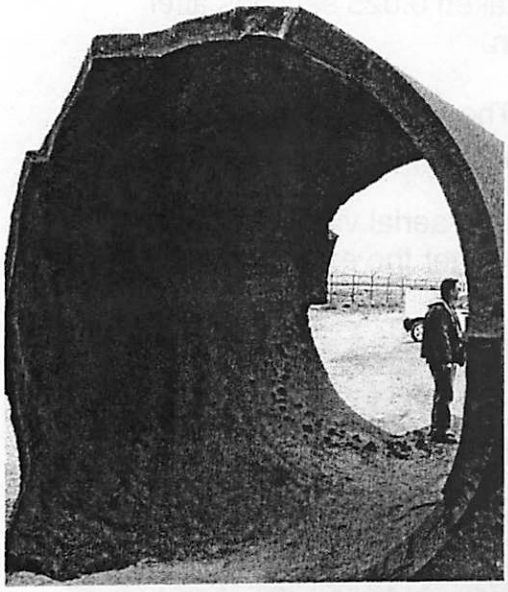

(left) "Jumbo" as of April 2007.

(bottom left) A replica of the "Fat Man" bomb that was detonated over Nagasaki.

(bottom right) The Trinity Test Site, April 2007. The obelisk seen to the left of the truck marks the spot of ground zero.

All pictures on this page courtesy of Jade Bond.

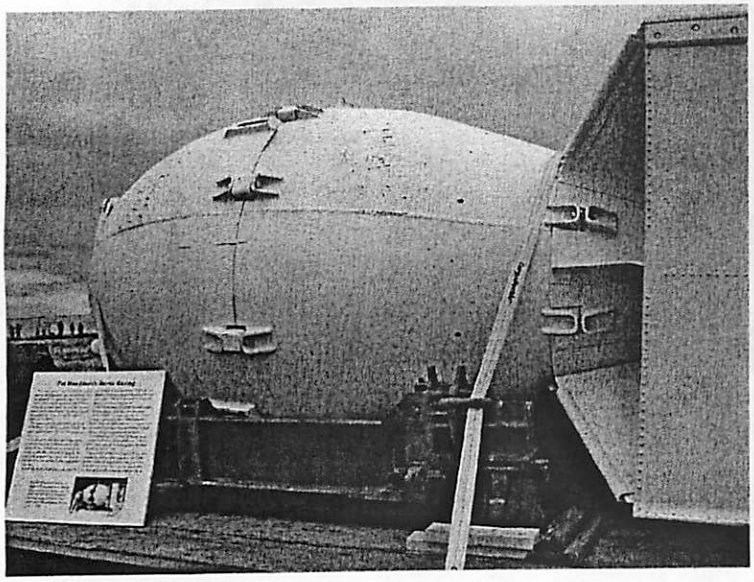

References

Numerous resources exist online, among which are...

http://www.wsmr.army.mil/pao/TrinitySite/trinph.htm
http://www.lanl.gov/history/atomicbomb/trinity.shtml
http://www.atomicarchive.com/Photos/Trinity/index.shtml
http://news.bbc.co.uk/2/hi/americas/4641861.stm
http://en.wikipedia.org/wiki/Trinity_test

The official report on the Trinity Test, the Smyth Report, can be found here--
http://www.atomicarchive.com/Docs/SmythReport/index.shtml

Emplacement of the Carrizozo lava flow

Fan Guo

General Introduction

The Carrizozo Lava flow field is a young, long basaltic flow field located in the Tularosa Basin which is eastern arm of the Rio Grande Rift in southern New Mexico. The flows consist of two basaltic lava flows, i.e., Upper and Lower Carrizozo Flows. The total length is $75km$, with the Lower Carrizozo Flow extending $50km$ south beyond the $25km$ long Upper Carrizozo Flow. It covers $330km^2$ with an estimated depth of $10-15$m, for a total erupted volume of about $4.3km^3$ [1]. The only identifiable source is the Little Black Peak cinder cone. The cone sits on a shallow shield which has a $2-5km$ diameter and $30-40m$ height. The lavas are intermediate in composition between alkalic and tholeiitic basalts and part of the volcanism associated with the Rio Grande rift [4].

The Carrizozo Lava flow is of interest because it is the longest lava flow in the U.S., including Hawaii, and has its original, well-preserved morphology. Meanwhile because of its obviously utility as a Mars analog. One particular problem of interest is why the Carrizozo Lava flows have such a long length. It is shown that a high effusion rate and tube-fed both contributed to the length of the Lower Carrizozo Flow, while the length of the flow is not related to topographic channeling, low viscosity or fissure-feeding of the flow [2, 3](see below for details).

Emplacement

There are a number of reasons for formation of long lava flows, such as, (1)low viscosity. (2)steep slop, (3)insulation by lava tubes or channels, (4)high eruption temperature, (5)high effusion rate, (6) a fissure source, etc. Keszthelyi and Pieri [3]examined these factors and suggested that the length of the flow is not related to topographic channeling, low viscosity or fissure-feeding of the flow, but rather to some other factor.

Lower-viscosity lavas (such as basalts) tend to form longer lava flows than more viscous lavas (such as andesites or rhyolites) factors cause low viscosity in basaltic melts: (1)high dissolved water content, (2)unusual major-element composition (3) high temperature. Chemical analyses and rock samples show no unusual bulk chemistry, vesicularity, crystal content, mineralogy or mineral textures when compared to other basaltic lava flows.

Quantitative calculation of rheology using empirical formula and theoretical model shows that Carrizozo lava was not dramatic different with other basaltic lava flows.

Fig 1.: Location and Shape of the Carrizozo Lava Flows

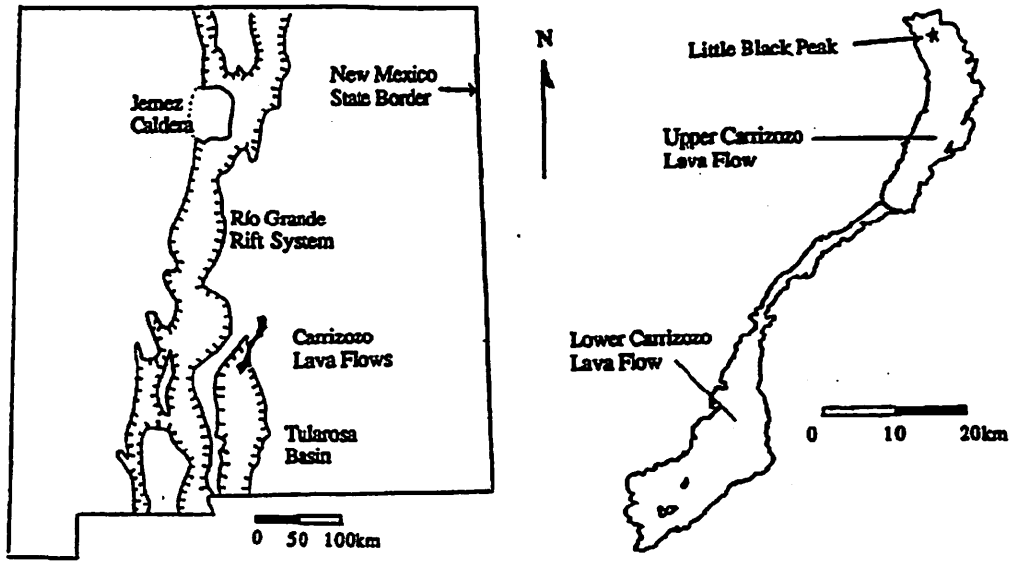

Table 1:Results for the Lower Carrizozo Flow.

	Range	Best Estimate
Temperature (°C):	1150 - 1200	1180
Viscosity (Pa/sec):	250 - 150	180
Yield Strength (Pa)		
Experimental:	5000 - 10	
Morphological:	1000 - 500	800
Flow Velocity (m/sec):	6 - 63	26
Effusion Rate (m^3/sec):	$7x10^4$ - $8x10^5$	$3x10^5$

From Keszthelyi and Pieri, (1989)

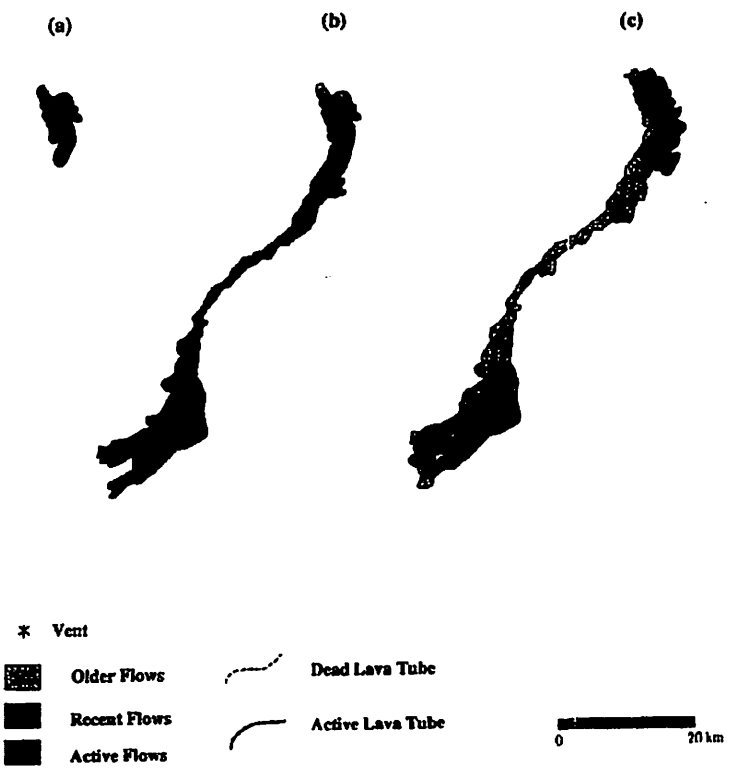

Fig. 7. Hypothetical emplacement history of the Carrizozo flow field based on the Kupaianaha flow field. (a) The initial eruption was probably centered around the present location of Little Black Peak. Lava flows may have attempted to advance in all directions from the source, but found motion down the shallow slope preferable. (b) For some length of time a large, stable, tube system developed through the narrow "neck" region of the flow field. This tube fed a series of sub-parallel, abutting flows to the south. (c) At some later point in time, this tube system broke down (possibly due to a longer pause in the eruption) and further flows built up around Little Black Peak, producing the topographic swell and radiating flow patterns observed in the present flow surface.

From Keszthelyi and Pieri, (1993)

Meanwhile there is nothing unusual about the chemistry composition. Effect of rheology on long-length of Carrizozo lava is probably negligible. It should be noted that the models and empirical correlations are only reliable to simple 'a'a flows. Thus here these techniques cannot give confident estimate of parameters.

By comparison between Carrizozo flow field and similarly large tube-fed pahoehoe Kupaianaha flow field on Hawaii. The authors [3] suggested that Carrizozo was emplaced as a long-duration, low effusion rate eruption. Using an effusion rate of 5 $m^3 s^{-1}$, it would take about 2-3 decades years to erupt the whole 4.3 km^3. Thus the single important factor in determining the length of the flow field is the long, undisturbed eruption duration. Another requirement to form such a long lava flow is that a long tube system must be maintained throughout most of the eruption.

While present models and empirical correlation for lava flows give a more reliable parametersin simple 'a'a flows case, the emplacement mechanism of pahoehoe lava flows are poorly known. Therefore more work should be made in future.

References

[1] Allen, JE., 1952, Roswell Geologic Society Guidebook, 5th Field Conference, pp. 9-11.

[2] Keszthelyi, L. P., & Pieri, D. 1990, Lunar and Planetary Institute Conference Abstracts, 21, 625

[3] Keszthelyi, L. P., & Pieri, D. 1993, Journal of Volcanology and Geothermal Research, 59, 59-75

[4] Renault, J., 1970, N.M. State Bur. Mines Miner. Resour., Circ. 113, Socorro, NM.

Inflation of Lava Flows

Colin Dundas

Physical Process

Inflation is the process of thickening a lava flow by injecting fluid lava under the cooled shell of a partially frozen lava flow. This occurs in almost all pahoehoe flows; inflated aa flows are also observed in some rare cases. In pahoehoe flows, flow lobes of decimeter to meter scale form and begin to crust over as the lava cools. Once thick enough, this crust can support hydrostatic pressure, and additional influx of lava causes the flow to inflate. This leads to lateral coalescence of flow lobes and also thickens the flow, sometimes by an order of magnitude or more. As the flow cools, some routes through the flow may evolve into lava tubes which feed the flow front.

This concept was alluded to by many early references and some lava flow features were explained using this mechanism, but it was first fully described and analyzed by Hon et al. (1994).

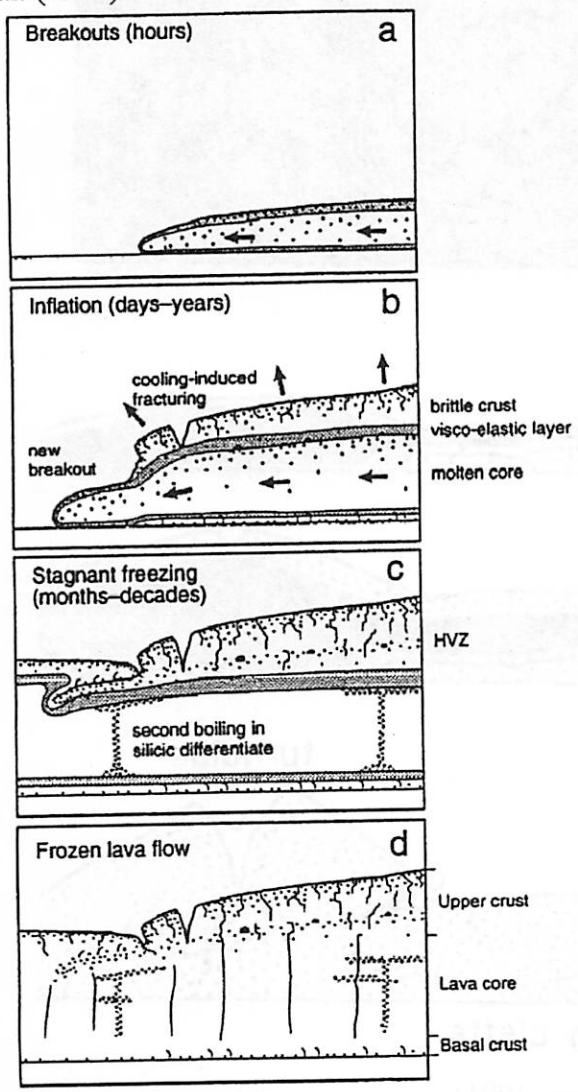

Fig. 1: Schematic of pahoehoe flow inflation (from Self et al., 1996)

Inflation Features

Inflation produces a variety of related landforms. **Lava rise plateaus** occur where a broad area has undergone inflation and been uplifted by a roughly constant amount. **Lava-rise pits** form when part of a flow is left behind as the surrounding surface rises. **Tumuli** are localized sites of greater-than-average inflation, which produce bulbous, fractured hummocks. (See Walker, 1991, for more detail). A common result of inflation is inversion of topography: initially high-standing areas tend to have a thin lava coating which cools and solidifies quickly, cutting off further injection of lava and inflation, while initially low areas may be sites of lava pooling and be subject to continuing inflation over longer periods of time.

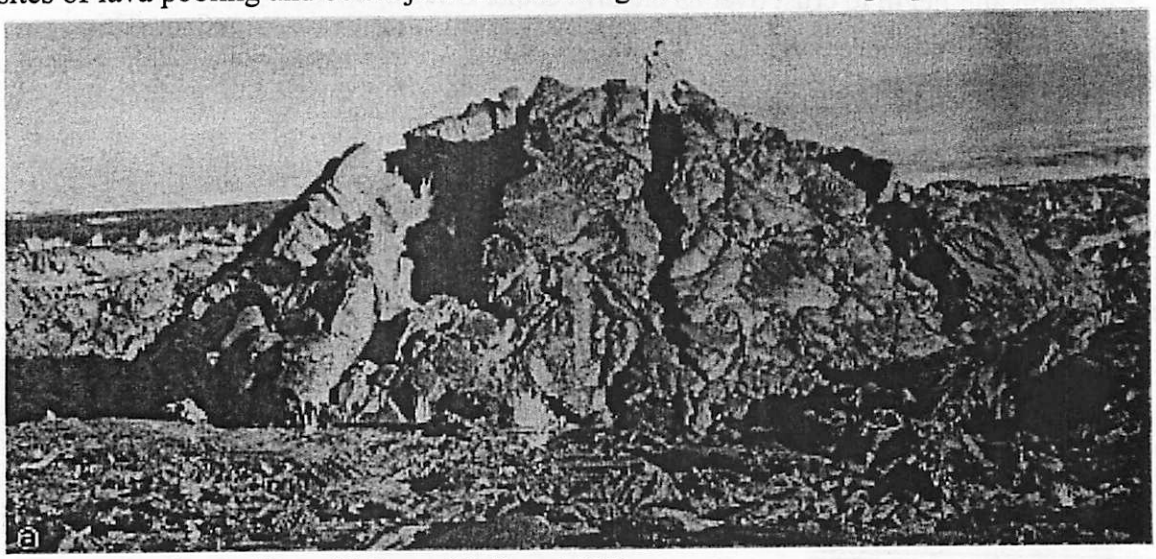

Fig. 2: Tumulus in Hawai'i (from Walker, 1991)

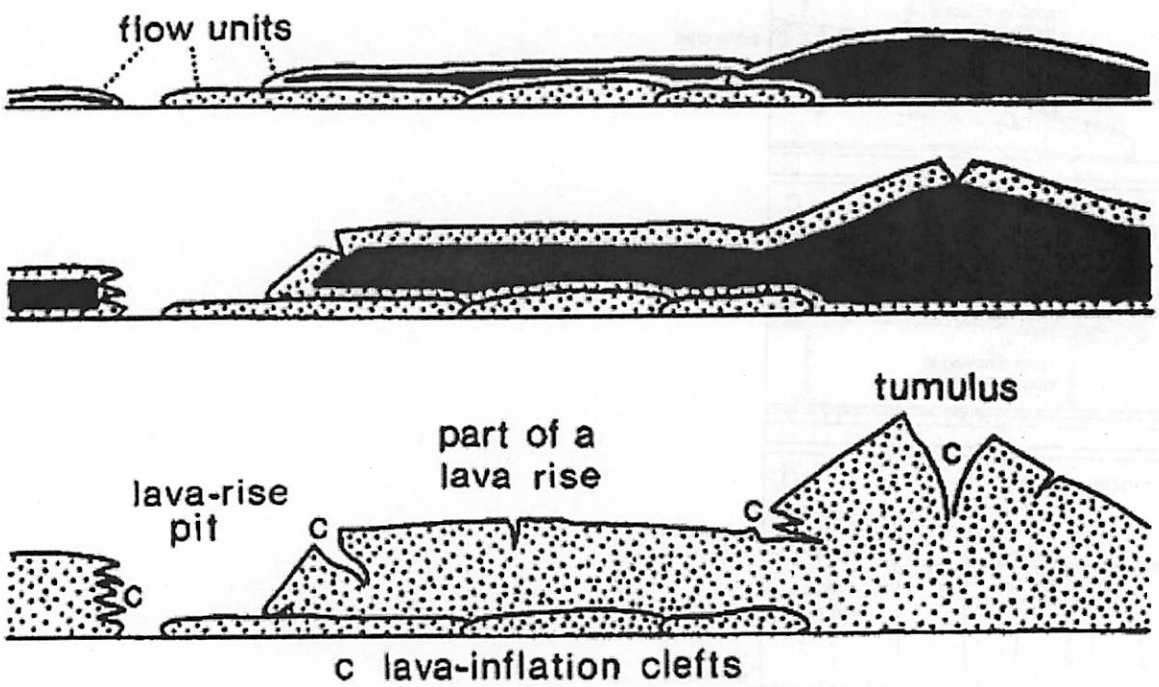

Fig. 3: Schematic of inflation features (from Walker, 1991)

At small scale, inflation leads to distinct and diagnostic patterns of vesicles. Inflated pahoehoe generally has a dense core and vesicular outer portion, possibly with pipe vesicles (P-type pahoehoe). "Blue-glassy" pahoehoe has a low-vesicularity outer layer and forms from residual lava held in an inflating flow long enough that bubbles coalesce. In cross-section, inflated flows will generally have a vesicular upper layer (generally ~50% of the total thickness) from the period of inflation, when fresh lava (and volatiles) was being delivered. Below this the lava will be massive, possibly with thin vesicular layers. Since the cooling rate of a basalt flow can be estimated by modeling, inflation timescales can be inferred.

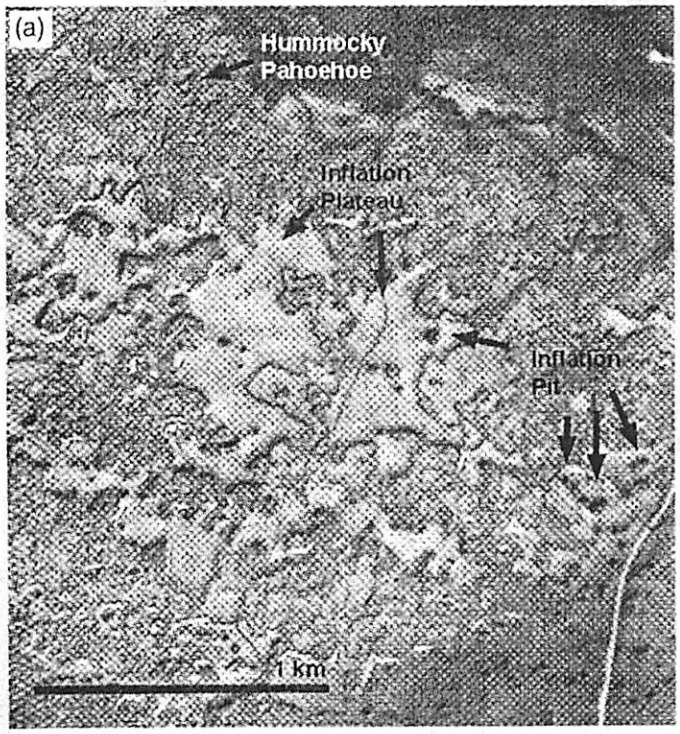

Fig. 4: Aerial view of inflation features on the Laki lava flow, Iceland (from Keszthelyi and McEwen, 2007)

Significance

The realization that lava flows (and pahoehoe in particular) grow by inflation has several important implications:

- Inflation means that the final thicknesses of lava flows differ from the initial emplacement. This must be taken into account when estimating flow parameters. A Bingham plastic rheologic model based on the final topography is invalid (and may be badly in error) in this case (Keszthelyi and Pieri, 1993).
- A large fraction of total lava volume is transported under an efficient insulating cover, assisting in the formation of very long lava flows (Self et al., 1998).
- Large lava flows (such as the Columbia River Basalts) reached their great thickness by inflation. This leads to substantially lower effusion rates and slower emplacement timescales of years rather than days. Since the eruption was slower, it need not have been turbulent, consistent with an origin as pahoehoe. (Self et al., 1996)

Planetary Observations

Inflation of lava flows should be more likely on bodies with lower gravity, since the weight of the crustal overburden will be reduced, as will the downslope force driving extension of the flow (Keszthelyi et al., 2000). However, eruption parameters of the flow (effusion rate, cooling rate, etc.) might also be systematically different.

Possible inflation-related features have been observed on Mars, including apparent inverted topography and lava-rise pits (Lanagan, 2004) and possible tumuli (e.g. Theilig and Greeley, 1986). One prominent surface morphology on Mars is "platy-ridged" lava, which is thought to form when a sheet flow crusts over and then is disrupted by a subsequent surge of lava under the crust, a mechanism similar but not identical to inflation. (Platy-ridged textures have recently been interpreted as frozen sea ice. Don't believe it.)

References

Hon, K., Kauahikaua, J., Denlinger, R., and Mackay, K. 1994. *GSA Bull.* 106, 351-370.

Keszthelyi, L., and McEwen, A. 2007. In Chapman, M. (Ed.), *The Geology of Mars: Evidence from Earth-based Analogs*, p. 126-150.

Keszthelyi, L. P., and Pieri, D. C. 1993. *J. Volc. Geotherm. Res.* 59, 59-75.

Keszthelyi, L., McEwen, A. S., and Thordarson, T. 2000. *J. Geophys. Res.* 105, 15027-15050.

Lanagan, P. 2004. Ph.D. Thesis, University of Arizona.

Self, S., Keszthelyi, L. P., and Thordarson, T. 1998. *Ann. Rev. Earth Planet. Sci.* 26, 81-110.

Self, S., Keszthelyi, L. P., and Thordarson, T. 2000. *Earth Planet. Sci. Let.* 179, 421-423.

Self, S., and 7 coauthors. 1996. *Geophys. Res. Let.* 23, 2689-2692.

Theilig, E., and Greeley, R. 1986. *J. Geophys. Res.* 91, E193-E206.

Walker, G. P. L. 1991. *Bull. Volcanol.* 53, 546-558.

Predictive models of lava flow paths

L. Ong

Motivation:
Predictive models of lava flow paths are developed primarily for hazard prediction and assessment. Models strive to determine the paths and probabilities that lava flows will intercept infrastructure and inhabited areas.

Lava flow basics:
Lava flows are gravitational currents composed of silicate liquid, crystals, and gas bubbles. As a flow progresses, the surface heat flux produces a thin surface layer of amorphous glass. This solid layer is emplaced most efficiently along the edges of the flow and creates solid crystallized levees. The flow typically becomes a channelized laminar flow.

The behavior, structure, and rate of the flow depend strongly on the properties of the magma, including the rate of effusion, viscosity of the flow (affected by the temperature, volatile content, and composition of the lava), the new environment in which the lava flows (air versus water), and the topography over and around which the flow travels.

Lava flow models therefore require appropriate knowledge of the flow characteristics in order to predict the distance a flow will travel before it solidifies and to usefully assess and mitigate these hazards. Given an *observed* flow, flow models attempt to predict flow shape, structure, and morphology, including unusual surface features such as large pancake domes and very long basalt flows.

Types of Models:

- Deterministic:
  - Predicts flow paths for a single specific eruption.
  - Modeled using topography, known input parameters for rheology and new environment.
  - Can be tested against flows that have occurred/will occur.
  - Examples:
    - Thermo-rheological model: Uses known effusion rate, viscosity, cooling rate, and topography measured for this specific flow. Only a single simulation is required (figure 1)
- Probabilistic:
  - Estimate probabilities that lava will flow along a certain path for all possible paths
  - Usually based on topography and temporal/spatial statistical distributions of historical flows
  - Examples:
    - Non-rheological: Lava sheds and catchments are areas within which lava flow will remain if it is erupted from a vent within that lava shed. These simple models require only topographic data and do not include physical details of the flow (fig. 2).
    - Thermo-rheological models: Simulations of lava flow paths including radiative cooling are performed for a range of rheological inputs (monte-carlo method). Multiple simulations are required to cover possible parameter space, but statistics of parameter space are based on historical flows.

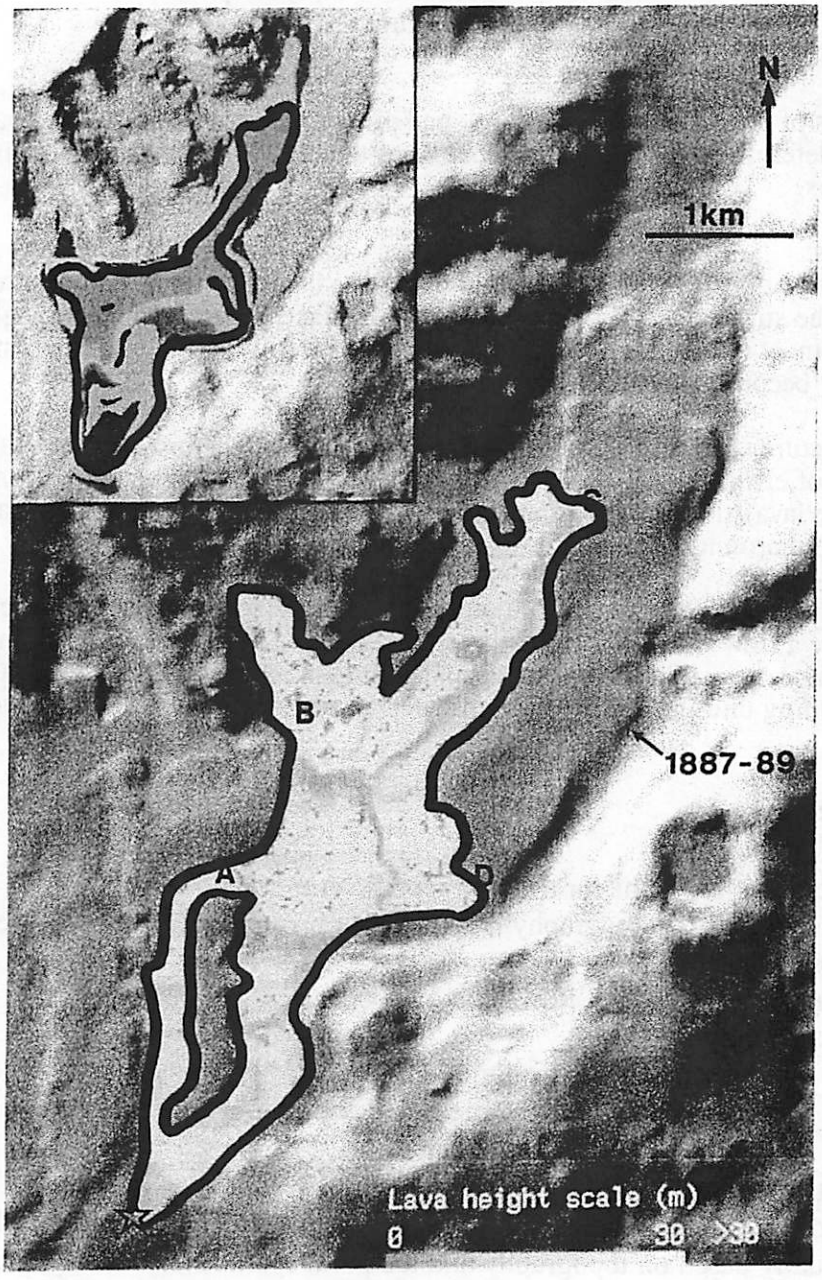

FIG 1:

Plate 1. FLOWFRONT simulation of the first 21 days of the Lonquimay, Chile, eruption of 1988-1989. The red to yellow colors show the variations in flow thickness of the simulated lava flow over a pseudo-illuminated image of the topography (lava flow of 1887-1889 is indicated). The inset image shows the various stages in the advance of the flow recorded by *Moreno and Gardeweg* [1989] (Table 1). The simulation volume (83 x 10^6 m^3) is equivalent to that represented by the lava flow at the dark red stage in the inset image. The letters A-D refer to locations described in the text. The vent is shown by the star.

FROM WADGE et al. (1994)

TABLE 3. Measurements of Fit Between a FLOWFRONT Simulation and the Lonquimay 1988-1989 Lava Flow

Volume 10^6 m^3	Iteration	Length			Area			Overlay Ratio
		Actual km	Simulation km	Ratio	Actual km^2	Simulation km^2	Ratio	
10	240	1.8	1.3	0.72	1.0	0.65	0.65	0.65
22	460	3.3	2.2	0.67	2.2	1.3	0.60	0.55
30	700	4.0	2.9	0.72	2.5	1.8	0.73	0.64
83	2340	6.3	5.8	0.92	5.5	4.6	0.84	0.68

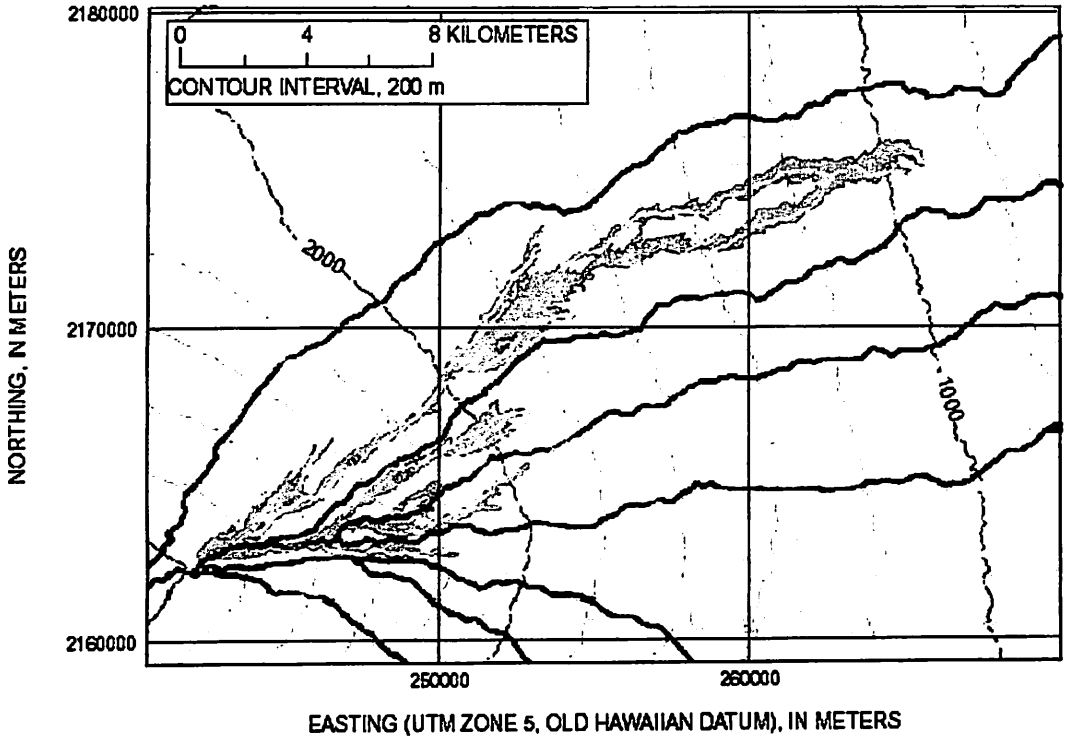

Fig. 2: 1984 Lava flows on Mauna Loa (shaded region). Black lines outline lava sheds, grey lines show estimated preferred lava pathways. From Kauahikaua (2001).

Implications:
Although lava flow models are used on Earth as hazard assessment tools, they can and should be used in planetary science contexts to investigate lava flow characteristics and the environmental conditions in which they were emplaced. This is easier said than done…

Discussion questions:

- Can predictive modeling help us interpret emplaced flows on Mars, Venus, and the Moon? Are the too many unknown flow parameters? How can we use current mission data to constrain input parameters?
- What about cryo-volcanoes? Are compositions different enough to allow better parameterization? How would modeling of cryo-volcanoes differ from terrestrial volcanism? Do we know enough to try to model them without ground/lander data?

References, additional reading:

Griffiths, R.W. (2000) "The Dynamics of Lava Flows." *Annual Reviews of Fluid Mechanics*. **32**, 477-518. (Great overview of lava flow characteristics)

Kauahikaua, J. *et al.* (2001). "Hawaiian Lava-Flow Dynamics During the Pu'u O'o Kupaianaha Eruption: A Tale of Two Decades." *USGS Professional Paper* no. 1676. (Overview of Hawaiian flows)

Wadge, P. A. *et al.* (1994). "Mapping lava flow hazards using computer simulation." *JGR*. **99** 489-504.

Fractal geometry of lava flow margins

David A. Minton

The mathematician Lewis Fry Richardson first noted that the measured length of the border between two countries was significantly different when measured at different scales [6]. He suggested the following empirical formula:

$$L \propto G^{1-D}, \tag{1}$$

which relates the length of the border, L, with the length of a straight line segment used to measure the border, G, and a dimensionless quantity D, that is always at least equal to unity. Benoît Mandelbrot extended Richardson's empirical work and called the quantity D the "fractional dimension," or *fractal* dimension [4]. Mandelbrot compared the measured fractal dimension of the jagged west coast of Britain with the smooth coastline of South Africa, along with several intermediate frontiers, shown in Fig. 1. One feature of fractals is that they exhibit self-similarity, that is features look similar at all scales. Fractals in nature are not true mathematical fractals, because they are finite in size and only exhibit fractal behavior over a limited range of scales [7].

Bruno et al. showed that the fractal nature of lava flows are correlated with silica content, with basaltic lava flows exhibiting fractal margins, but not silicic lava flows [1, 2]. This difference corresponds to a difference in rheology and emplacement mechanism, rather than directly due to composition. For instance, he showed that pahoehoe basalts have fractal dimensions in the range of $D = 1.13-1.23$, whereas a'a basalts are typicaly $D = 1.05-1.09$, even though the same basaltic composition can lead to either pahoehoe or basalt (see Fig. 2). This suggests that higher values of D correlate with lower viscosity.

Kauhanen measured the fractal dimensions of seven martian lava flows and showed that they exhibited fractal behavior, though there was not a good linear fit to the measured fractal dimension [3]. This may have been due to resolution limitations of the Viking imagery available at the time, and higher resolution imagery of martian lava flows margins may be needed for practical fractal margin analysis [5]. The ejecta and outflows of craters on Venus also exhibit fractal behavior [7, 8].

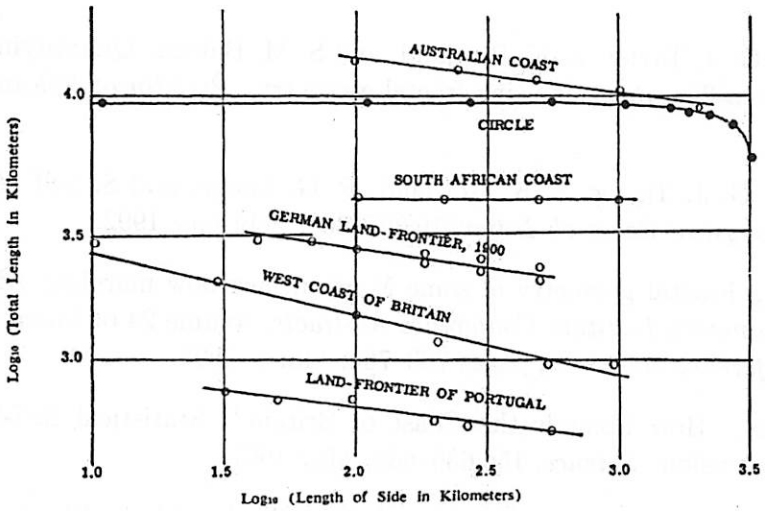

Figure 1: Richardson plot of several coastlines and frontiers showing ranges of fractal dimension. For comparison, a non-fractal shape (circle) is shown.

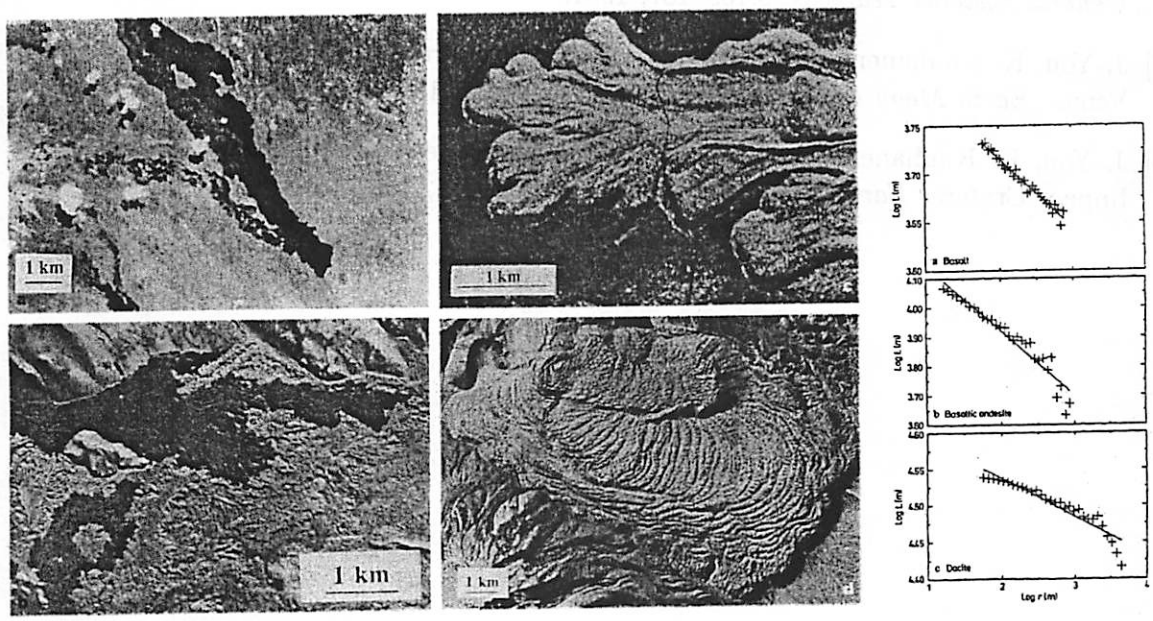

Figure 2: *Left:* Plan-view shapes of lava flows of various compositions (in order of increasing silica content): *a* basalt (Galapago Islands); *b* basaltic andesite (Hekla, Iceland); *c* andesite (Mount Shasta, US); *d* dacite (Chao, Chile). As silica content increases, flow lobes tend to widen, thicken and protrude less from the main mass of the lava flow, and the smaller-scale features become suppresed. *Right:* Richardson plots of representative *a* a'a basalt (Galapagos Islands); *b* basaltic andesite (Hekla, Iceland); *c* dacite (Chao, Chile), based on image data. Note that the date in (a) are closely approximated by a straight line, whereas teh data for the higher silica flows (b,c) are not linear. [1]

References

[1] B. C. Bruno, G. J. Taylor, S. K. Rowland, and S. M. Baloga. Quantifying the effect of rheology on lava-flow margins using fractal geometry. *Bulletin of Volcanology*, 56:193–206, 1994.

[2] B. C. Bruno, G. J. Taylor, S. K. Rowland, P. G. Lucey, and S. Self. Lava flows are fractals. *Geophysical Research Letter*, 19:305–308, February 1992.

[3] K. Kauhanen. Fractal geometry of some Martian lava flow margins: Alba Patera. In *Lunar and Planetary Institute Conference Abstracts*, volume 24 of *Lunar and Planetary Institute Conference Abstracts*, pages 763–764, March 1993.

[4] B. Mandelbrot. How Long Is the Coast of Britain? Statistical Self-Similarity and Fractional Dimension. *Science*, 156:636–638, May 1967.

[5] L. M. Norman. Use of Fractal Geometry for the Study of Lava Flows. In *Lunar and Planetary Institute Conference Abstracts*, volume 31 of *Lunar and Planetary Institute Conference Abstracts*, pages 1338–+, March 2000.

[6] L. F Richardson. The problem of contiguity: an appendix of statistics of deadly quarrels. *General Systems Yearbook*, 6:139–187, 1961.

[7] J. You, K. Kauhanen, and J. Raitala. Fractal Properties of Crater Ejecta Outlines on Venus. *Earth Moon and Planets*, 71:9–31, November 1995.

[8] J. You, K. Kauhanen, and J. Raitala. Fractal Properties of Outflows from Venusian Impact Craters. *Earth Moon and Planets*, 73:195–214, June 1996.


Snowflake
St Johns
Taylor
Pine
Payson
Show Low
Pinetop-Lakeside
Eagar
Young
Cibecue
McNary
Whiteriver
Reserve
Magdalena
Socorro
Mountainair
Corona
Carrizozo
Capitan
Ruidoso
Mescalero
Tularosa
La Luz
Cloudcroft
Alamogordo
Timberon
Elephant Butte Reservoir State Park
Truth Or Consequences
Williamsburg
Salem
Hatch
Las Cruces
Aguirre Springs National Rec Area
Chaparral
Canutillo
Sunland Park
El Paso
Socorro
San Elizario
Fabens
Tornillo
Fort Hancock
Sierra Blanca
Columbus
Ascensión
Apache Junction
Miami
Globe
San Carlos
Peridot
Superior
Kearny
Florence
Bylas
Clifton
Pima
Thatcher
Safford
Duncan
Silver City
Bayard
Hurley
Mammoth
Oracle
San Manuel
Oro Valley
Marana
Tucson
Saguaro National Park-East
Vail
Green Valley
Benson
St David
Tombstone
Huachuca City
Sierra Vista
Bisbee
Douglas
Naco
Nogales
Nogales
Cananea
Lordsburg
Deming
Willcox
Vado
Whitesands National Monument
87
60
260
180
191
12
54
70
77
79
10
19
25
380
82
62
375
23
2
14
15

Kenzin
Afton
Rutter
Lanark
NM 9
Columbus Rd
Strauss
136
Pete V Domenici Hwy
Chamberino
El Ojito
El Camino Real
28
La Union
Alvarez Rd
McNutt Rd
273
182
225
Washington St
478
Orange
Santa Teresa
Lizard
Westside Dr
184
Prado Verde
Berino
New Mexico
Texas
Borderland
Canutillo
Talbot Ave
Nomay
Vinton
Westway
Anthony
Hacienda Acres
Anthony Dr
460
404
S Main St
Doniphan Dr
20
Montoya
10
Woodrow B
N Resler Dr


2000 ft
1 km


500 ft
200 m